

Article

# Numerical Study on the Hydrodynamic Characteristics of a Double-Row Floating Breakwater Composed of a Pontoon and an Airbag

Xiaofei Cheng <sup>1</sup> , Chang Liu <sup>1</sup>, Qilong Zhang <sup>2</sup>, Ming He <sup>2,3,\*</sup>  and Xifeng Gao <sup>2,\*</sup>

<sup>1</sup> School of Civil and Ocean Engineering, Jiangsu Ocean University, Lianyungang 222005, China; chengxiaofei@jou.edu.cn (X.C.); 2018120665@jou.edu.cn (C.L.)

<sup>2</sup> School of Civil Engineering, Tianjin University, Tianjin 300350, China; 206086@tju.edu.cn

<sup>3</sup> Shandong Provincial Key Laboratory of Ocean Engineering, Ocean University of China, Qingdao 266100, China

\* Correspondence: minghe@tju.edu.cn (M.H.); gaoxifeng@tju.edu.cn (X.G.)

**Abstract:** By adding a cylindrical airbag on the leeward side of a cuboid pontoon, a new-type double-row floating breakwater is designed to improve the wave attenuation performance, and its hydrodynamic characteristics are studied through numerical simulations. First, based on the smoothed particle hydrodynamics (SPH) method, a numerical model used to simulate the interaction between waves and moored floating bodies is built. The fluid motion is governed by the Navier–Stokes equations. The motion of the floating body is computed according to Newton’s second law. The modified dynamic boundary condition is employed to treat the solid boundary. The lumped-mass method is adopted to implement the mooring system. Then, two physical model experiments on waves interaction with cuboid and dual cylindrical floating pontoons are reproduced. By comparing the experimental and numerical wave transmission coefficients, wave reflection coefficients, response amplitude operators and mooring force, the reliability of the numerical model is validated. Finally, the validated numerical model is applied to study the influence of separation distance and wave parameters on the hydrodynamic characteristics of the double-row floating breakwater. The results indicate that the optimal separation distance between pontoon and airbag is 0.75 times the wavelength. At such separation distance and within the concerned 1–4 m wave heights and 4–7 s wave periods, the pontoon-airbag system presents better wave attenuation performance than a single pontoon. This improvement weakens as wave height increases while it strengthens as the wave period increases. In addition, the double-row floating breakwater is more effective in a high-wave regime than in a low-wave regime. In the case of short waves, attention should be paid to the stability and mooring reliability of the seaward pontoon, while in the case of long waves, care needs to be taken of the leeward airbag.

**Keywords:** floating breakwater; wave transmission coefficient; response amplitude operator; mooring force; smoothed particle hydrodynamics (SPH)



**Citation:** Cheng, X.; Liu, C.; Zhang, Q.; He, M.; Gao, X. Numerical Study on the Hydrodynamic Characteristics of a Double-Row Floating Breakwater Composed of a Pontoon and an Airbag. *J. Mar. Sci. Eng.* **2021**, *9*, 983. <https://doi.org/10.3390/jmse9090983>

Academic Editor:  
Alessandro Antonini

Received: 1 August 2021  
Accepted: 3 September 2021  
Published: 8 September 2021

**Publisher’s Note:** MDPI stays neutral with regard to jurisdictional claims in published maps and institutional affiliations.



**Copyright:** © 2021 by the authors. Licensee MDPI, Basel, Switzerland. This article is an open access article distributed under the terms and conditions of the Creative Commons Attribution (CC BY) license (<https://creativecommons.org/licenses/by/4.0/>).

## 1. Introduction

Breakwaters are coastal engineering structures used to provide safe harborage and reduce coastal erosion. Compared with conventional seated breakwaters, floating breakwaters have the merits of faster construction, lower requirement of seabed conditions, less hindering water circulation, weaker influence of tidal fluctuation and more aesthetic pleasure [1]. Therefore, they have been very popular and exhibited enormous potential for engineering applications.

Floating breakwaters attenuate incident waves mainly through wave reflection and energy dissipation. The cuboid pontoon [2] (Figure 1a) and cylindrical pontoon [3] (Figure 1b) are the simplest and most classical types. To enhance the wave reflection, Gesraha [4] added

two vertical plates on the bottom edge of the cuboid pontoon and thereby constructed a  $\Pi$ -type floating breakwater (Figure 1c). The number and position of the vertical plates were further optimized by Koraim and Rageh [5] (Figure 1d). To increase the energy dissipation, Koo [6] and He et al. [7] added air chambers in the middle (Figure 1e) and to lateral sides (Figure 1f) of the cuboid pontoon, respectively. Through converting wave energy to electricity, the transmitted wave was efficiently attenuated. Wang and Sun [8] assembled diamond blocks into a permeable floating breakwater (Figure 1g). Due to the enhanced surface friction and turbulent flow motion, energy dissipation of the permeable floating breakwater is significant. In addition, some measures can both increase the wave reflection and energy dissipation. For example, Mani [9] designed a Y-type floating breakwater by connecting a row of pipes to the bottom of a trapezoidal pontoon (Figure 1h). The results showed that more than 50% of the incident wave could be attenuated even if the length of the Y-type floating breakwater was only 0.15 times the wavelength. Similarly, Nasri et al. [10] attached porous plates to the bottom of the trapezoidal pontoon (Figure 1i), and found that increasing the number and height of the plates, reducing the porosity of the seaward plate and increasing the porosity of leeward plates were all beneficial to the hydrodynamic performance of the floating breakwater. Dong et al. [11] proposed a horizontal plate-net floating breakwater (Figure 1j) and measured the effects of the length and stiffness of the horizontal plate as well as the net spacing on the wave transmission coefficient.

The above work was dedicated to improving the wave attenuation performance by altering the geometry of the single floating body. Since wave attenuation performance is closely related to the ratio of structural length to wavelength, deploying multiple floating bodies is a more intuitive approach. For a rigidly connected dual cuboid pontoon floating breakwater (Figure 1k), Williams and Abul-Azm [12] investigated the influence of width, draft, interspacing and mooring stiffness on the wave reflection coefficient. Ji et al. [13] measured the hydrodynamic characteristics of a rigidly connected dual cylindrical pontoon floating breakwater (Figure 1l) and compared it with porous and net cage floating breakwaters. To further improve the wave attenuation performance, Ji et al. [14] attached one or more layers of nets to the bottom of the dual pontoon (Figure 1m) and optimized the number, height and porosity of the nets. A triple cuboid floating pontoon floating breakwater (Figure 1n) was also analyzed by Syed and Mani [15].

Building composite structures, no matter a single body with complex geometry and rigidly connected multiple bodies, is difficult and expensive. As an alternative, another floating body can be added to constitute a double-row floating breakwater. This approach improves the wave attenuation performance not only by increasing the total length of the structure but also by utilizing the hydrodynamic interference between floating bodies. As far as we know, there are only a few studies on the double-row floating breakwater. Williams et al. [16] investigated the influence of wave and structural parameters on the wave reflection properties of a pair of cuboid pontoons (Figure 1o). Ji et al. [17] compared the hydrodynamic performance of double-row and single-row composite structures composed of two cuboid pontoons at the ends and a mesh cage in the middle (Figure 1p). The results indicated that the eddy losses and moon pool effect made the double-row floating breakwater more effective, and the separation distance between pontoons significantly affect the wave attenuation performance and mooring force. Similarly, Ji et al. [18] compared the hydrodynamic performance of double-row and single-row composite structures composed of two cylindrical pontoons and a mesh cage suspended below (Figure 1q). The double-row floating breakwater was found to exhibit better wave attenuation performance, especially in short-wave and high-wave regimes.

In the above studies, pontoons were used on both seaward and leeward sides, which in fact is not sensible, at least from two aspects. First, the pontoon is solid and reliable and therefore can be arranged on the seaward side to resist wave impact. Since part of the wave energy is blocked by the pontoon, it is more appropriate to place a less durable and more economical structure such as an airbag filled with ballast water on the leeward side. Second, for floating pontoons that have already been built, it is more convenient to

add one row of maneuverable airbags than bulky pontoon to temporarily improve the wave attenuation performance. Before applying the pontoon-airbag system in engineering practice, it must be well designed based on a systematically hydrodynamic analysis to obtain the greatest cost-effectiveness. However, no relevant research has been carried out. By optimizing the separation distance between pontoon and airbag and investigating the hydrodynamic characteristics under various wave conditions, this paper aims to provide a scientific basis for the engineering application of the double-row floating breakwater composed of a pontoon and an airbag.

Computational fluid dynamics methods have been widely used to study the hydrodynamic characteristics of floating breakwaters. Under the potential flow theory, Duan et al. [19] conducted a boundary element method (BEM)-based study on the principal dimensions of a F-type floating breakwater (Figure 1r). Vijay et al. [20] analyzed the wave scattering over an array of trapezoidal porous pontoons (Figure 1s) with the dual BEM. The scaled boundary finite element method was used by Fouladi et al. [21] to solve the interaction between waves and moored floating breakwaters with arbitrary cross-sections in an infinite fluid domain. Under the viscous flow theory, Peng et al. [22] simulated the nonlinear interaction between waves and submerged floating breakwaters by using the finite difference method (FDM). Qu et al. [23] applied the FDM-based open-source code REEF3D to investigate the sheltering effects of a floating breakwater on a bridge deck subjected to cnoidal waves. Zhan et al. [24] used the commercial software FLUENT, which is based on the finite volume method (FVM), to model the interaction between regular/irregular waves and T-type fixed and floating breakwaters (Figure 1t), respectively. Another FVM-based software, Star-CCM+, was utilized by Zhang et al. [25] to examine the hydrodynamic performance of a wave energy converter-type floating breakwater under regular waves.

The smoothed particle hydrodynamics (SPH) method [26–30] is a Lagrangian meshfree numerical scheme that was originally developed for solving astrophysical problems [31,32] and has been later extended to a wide variety of problems involving single-phase and multi-phase fluid [33,34], Newtonian and non-Newtonian fluid [35], elastic and plastic dynamics [36,37], explosion [38], electromagnetics [39], etc.

Compared with the conventional mesh-based numerical schemes, the SPH method is more convenient for handling boundaries and interfaces with complex geometry, large deformation, and irregular motion. Thus, it has been attracting much research interest from the coastal and ocean engineering community. Typical applications are the wave/current-structure interaction [40–42], wave deformation over topography [43–45], liquid sloshing [46–48], renewable energy utilization [49–51] and sediment dynamics [52–54], and the reader is referred to the review papers [55–57] to see more examples. Herein, the SPH method is applied to investigate the pontoon-airbag double-row floating breakwater due to the feature of the physical problem. The floating breakwater oscillates in the wave field and meanwhile drifts from the initial position caused by the mean drift force. The motion of the floating breakwater, in turn, alters the wave field, leading to a more complicated free surface. These phenomena are what the SPH method excels at. In addition, several SPH open-source codes have been developed in recent years, such as the efficiency/economy-optional DualSPHysics [58], the algorithm-inclusive SPlisHSPlasH [59] and the industry-oriented SPHinXsys [60]. The present study was carried out by using an in-house code that originated from the classic SPHysics [61].

Historically, breakwaters have been addressed with the SPH method many times. For seated breakwaters, Rogers et al. [62] simulated the wave striking a caisson-type breakwater sitting on an impermeable foundation by using SPHysics [61]. The computed sliding displacement of and the horizontal wave force on the caisson were in reasonable agreement with the experimental data from Wang et al. [63]. Akbari and Taherkhani [64] further showed that, by considering the permeability of the foundation, the computed displacement was in better agreement with the experimental data. Altomare et al. [65] modeled the interaction between waves and rubble-mound breakwaters by using Dual-

SPHysics [58]. DualSPHysics [58] was also applied by Zhang et al. [66] to compute the wave run-ups on a breakwater seated in Chongwu town, China, using the realistic wave conditions, bathymetry and dimensions. By combining the SPH method and the discrete element method, Ren et al. [67] and Sarfaraz and Pak [68] investigated the wave profiles, velocity fields and hydraulic pressure near the armor blocks laid on the slope breakwaters. Moreover, the stability of the armor layers during wave attacks was inspected.

As for floating breakwaters, Shao and Gotoh [69] simulated the coupled motion between regular waves and a curtain-wall breakwater (Figure 1u) by bringing the large eddy simulation technology into the Incompressible SPH (ISPH) model. Delavari and Gharabaghi [3] evaluated the wave transmission coefficients, wave reflection coefficients and heave responses of a pile-moored floating breakwater at different drafts and water depths. By using SPHysics [61] and by simplifying the mooring system as massless linear springs, Ren et al. [70] analyzed the influence of structural length, density and immersion depth on the hydrodynamic performance of a submerged floating breakwater. Domínguez et al. [71] modeled the interaction between waves and moored floating bodies by incorporating the open-source mooring library MoorDyn [72] into DualSPHysics. Afterward, the coupled DualSPHysics-MoorDyn was applied by Liu and Wang [73] to compare the hydrodynamic performance of floating breakwaters with six different cross-sections (Figure 1v). Most recently, Cui et al. [74] compiled the open-source mooring analysis program MAP++ [75] into the SPH code to predict the hydrodynamic performance of a multi-module floating breakwater.

Not only floating breakwaters, the SPH method was also utilized for other kinds of moored floating bodies. Gunn et al. [76] modeled the vertical and horizontal oscillations of a tethered spherical buoy in still water as well as its motion responses subjected to regular wave excitations. Pan et al. [77] computed the fluid force acting on and the movement behavior of a simplified semi-submersible floating platform due to solitary wave attack. In more detail, Rudman and Cleary [78] studied the rogue wave impact on a realistic semi-submersible floating platform, focusing on the influence of mooring layout on the platform motion and mooring force. By implementing catenary equations into DualSPHysics, Barreiro et al. [79] simulated the wave-induced motion of a wind turbine base moored by three spread lines. Using the same approach, Crespo et al. [80] analyzed the hydrodynamic characteristics of a floating oscillating water column converter in a regular wave field. Ardianti et al. [81] coupled the ISPH method and the extended distinct element method to investigate the tsunami wave force on and the movement behavior of floating shelters with different structural shapes and mooring layouts.

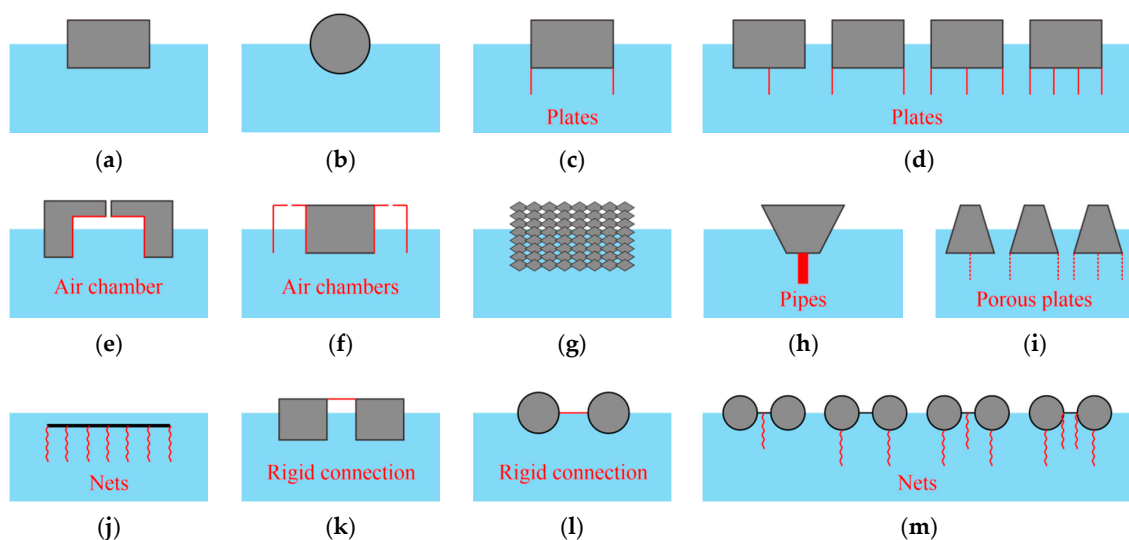
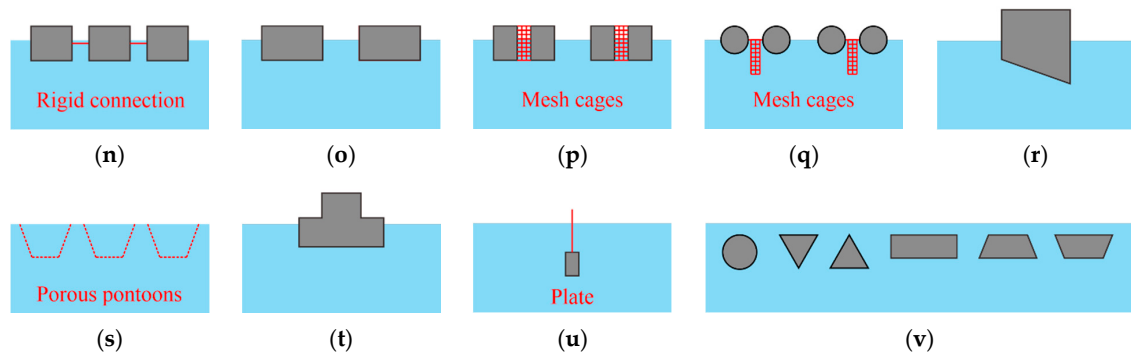


Figure 1. Cont.



**Figure 1.** Different types of floating breakwaters: (a) Cuboid pontoon [2]; (b) Cylindrical pontoon [3]; (c)  $\Pi$ -type pontoon [4]; (d) Cuboid pontoon-plates [5]; (e) Pontoon with an air chamber [6]; (f) Pontoon with two air chambers [7]; (g) Permeable structure [8]; (h) Y-Type pontoon [9]; (i) Trapezoidal pontoon-porous plates [10]; (j) Horizontal plate-nets [11]; (k) Dual cuboid pontoon [12]; (l) Dual cylindrical pontoon [13]; (m) Dual cylindrical pontoon-nets [14]; (n) Triple cuboid pontoons [15]; (o) Double-row cuboid pontoons [16]; (p) Double-row cuboid pontoons-mesh cage [17]; (q) Double-row cylindrical pontoons-mesh cage [18]; (r) F-type pontoon [19]; (s) Trapezoidal porous pontoons [20]; (t) T-type pontoon [24]; (u) Curtain wall [69]; (v) Pontoon with different cross-sections [73].

This paper is organized in the following manner. After the introduction, Section 2 briefly introduces the SPH-based numerical model. Then, in Section 3, the numerical model is validated by reproducing physical model experiments on waves interaction with the cuboid and dual cylindrical floating pontoons, respectively. The validated numerical model is finally applied in Section 4 to study the influence of separation distance and wave parameters on the hydrodynamic characteristics of a prototype double-row floating breakwater composed of a cuboid pontoon and a cylindrical airbag.

## 2. Numerical Model

The numerical model is outlined in this section, mainly including the equations of fluid motion and floating body motion and the methods of solid boundary treatment and mooring system implementation.

### 2.1. Fluid Equations

The fluid motion is governed by the Navier–Stokes equations composed of the continuity equation and the momentum equation. In the  $\delta$ -SPH framework, they can be discretized, respectively, as [82,83]

$$\frac{D\rho_i}{Dt} = -\rho_i \sum_j (\mathbf{u}_j - \mathbf{u}_i) \cdot \nabla_i W_{ij} V_j + 2\delta h c_0 \sum_j \psi_{ji} \frac{(\mathbf{r}_j - \mathbf{r}_i) \cdot \nabla_i W_{ij}}{\|\mathbf{r}_j - \mathbf{r}_i\|^2} V_j \quad (1)$$

$$\mathbf{r}_i = \frac{D\mathbf{u}_i}{Dt} = -\frac{1}{\rho_i} \sum_j (p_j + p_i) \nabla_i W_{ij} V_j + \mathbf{g} + \alpha h c_0 \frac{\rho_0}{\rho_i} \sum_j \pi_{ij} \nabla_i W_{ij} V_j \quad (2)$$

where subscripts  $i$  and  $j$  denote the target and neighboring particles, respectively;  $t$  is the time;  $\mathbf{g}$  is the gravitational acceleration;  $\rho$ ,  $p$ ,  $V$ ,  $\mathbf{u}$  and  $\mathbf{r}$  are the density, pressure, volume, velocity and position, respectively;  $\rho_0 = 1000 \text{ kg/m}^3$  is the reference density;  $h = 1.5 \delta_p$  is the smoothing length with  $\delta_p$  being the initial particle spacing;  $\delta = 0.1$  is the diffusion coefficient;  $\alpha = 8 \nu / (h c_0)$  is the artificial viscosity coefficient with  $\nu$  being the kinematic viscosity of fluid and  $c_0$  being the numerical speed of sound. Its value, in this study, varies between  $2.7 \times 10^{-7}$  and  $2.4 \times 10^{-5}$  depending on different cases;  $W$  is the Wendland C2 kernel function [84] defined as:

$$W = \frac{7}{4\pi h^2} \left(1 - \frac{\Delta r}{2h}\right)^4 \left(\frac{2\Delta r}{h} + 1\right) \quad 0 \leq \Delta r \leq 2h \quad (3)$$

where  $\Delta r$  is the transient particle spacing.

The last term in Equation (1) is a density diffusion added to reduce the numerical noise that affects the stability of the density field, where  $\psi_{ij}$  has the following expression:

$$\psi_{ij} = (\rho_j - \rho_i) - \frac{1}{2} \left( \langle \nabla \rho \rangle_j^L + \langle \nabla \rho \rangle_i^L \right) \cdot (\mathbf{r}_j - \mathbf{r}_i) \tag{4}$$

$$\langle \nabla \rho \rangle_j^L = \sum_j (\rho_j - \rho_i) \left[ \sum_j (\mathbf{r}_j - \mathbf{r}_i) \otimes \nabla_i W_{ij} V_j \right]^{-1} \nabla_i W_{ij} V_j \tag{5}$$

The last term in Equation (2) is an artificial viscosity also aiming at stabilizing the numerical scheme and meanwhile providing numerical fluid viscosity, where  $\pi_{ij}$  has the following expression:

$$\pi_{ij} = \frac{(\mathbf{u}_j - \mathbf{u}_i) \cdot (\mathbf{r}_j - \mathbf{r}_i)}{\|\mathbf{r}_j - \mathbf{r}_i\|^2} \tag{6}$$

Equations (1) and (2) are closed by introducing a linearized equation of state written as:

$$p_i = c_0^2 (\rho_i - \rho_0) \tag{7}$$

The explicit Symplectic scheme [61] with second-order accuracy is used to solve Equations (1) and (2), and a variable time step [85] considering particle acceleration, viscous fluid diffusion and CFL condition is adopted to guarantee the stability of numerical integration. The formula for the variable time step is given as follows:

$$\Delta t = \min \left[ 0.25 \sqrt{\frac{h}{\max_i (d\mathbf{u}_i/dt)}}, 0.125 \frac{h^2}{\nu}, 0.5 \min_i \left( \frac{h}{c_0 + h \max_j \pi_{ij}} \right) \right] \tag{8}$$

### 2.2. Floating Body Equations

For computational convenience, both pontoon and airbag are assumed to be rigid and their mass distribution does not change with the floating body motion. Thus, the translation and the rotation around the center of mass can be calculated by:

$$M \frac{d\mathbf{V}}{dt} = \mathbf{F}_f + \mathbf{F}_m + M\mathbf{g} \tag{9}$$

$$I \frac{d\boldsymbol{\Omega}}{dt} = \mathbf{T}_f + \mathbf{T}_m \tag{10}$$

where  $M$ ,  $I$ ,  $\mathbf{V}$  and  $\boldsymbol{\Omega}$  are the mass, moment of inertia, linear and angular velocities of the floating body, respectively;  $\mathbf{F}_f$  and  $\mathbf{T}_f$  are the fluid force acting on the floating body and its torque to the center of mass, respectively;  $\mathbf{F}_m$  and  $\mathbf{T}_m$  are the mooring force and its torque to the center of mass, respectively.

#### 2.2.1. Solid Boundary Treatment

The solid boundary is treated by using the modified dynamic boundary condition [86]. Two rows of dynamic boundary particles (DBPs) are fixed on the contours of numerical wave flume and floating body. They participate in the computations of the continuity equation, but the obtained densities are corrected by the averaged densities of neighboring fluid particles. That is:

$$\tilde{\rho}_k = \chi \rho_k + (1 - \chi) \bar{\rho}_i \tag{11}$$

where  $\rho_k$  and  $\tilde{\rho}_k$  are the original and corrected densities of DBP labeled as  $k$ , respectively;  $\bar{\rho}_i$  is the averaged density of the fluid particles in the kernel support of DBP  $k$ .  $\chi$  is a weight coefficient, which mainly depends on the intensity of hydrodynamic force acting on the solid boundary, the type of kernel function and the smoothing length. On the one hand, a smaller  $\chi$  leads to a smooth pressure field near the solid boundary, but the repulsive force

exerted by the solid boundary can be inadequate, which perhaps results in the penetration of fluid particles. On the other hand, a greater  $\chi$  effectively prevents the particle penetration but gives rise to a fluctuating pressure field which results in unphysical repulsion and adhesion of fluid particles near the solid boundary. Based on the sensitivity analysis as well as our considerable experience in the past studies [51,70,86–88],  $\chi$  should be within 0–0.5 range and 0.2 is a proper choice for simulating waves interaction with floating bodies.

In Equation (11),  $\bar{\rho}_i$  is calculated by:

$$\bar{\rho}_i = \frac{1}{N_p} \sum_{i=1}^{N_p} \left[ \rho_i + \frac{\partial \rho}{\partial z} (z_i - z_k) \right] \tag{12}$$

where  $N_p$  is the total number of fluid particles  $i$  in the kernel support of DBP  $k$ ;  $z$  is the vertical position of the particle. According to Equation (7), we have:

$$\frac{\partial \rho_i}{\partial z} = \frac{1}{c_0^2} \frac{\partial p_i}{\partial z} = \frac{\rho_0 g}{c_0^2} \tag{13}$$

By substituting Equations (12) and (13) into Equation (11), it obtains:

$$\tilde{\rho}_k = \chi \rho_k + (1 - \chi) \frac{1}{N_p} \sum_{i=1}^{N_p} \left[ \rho_i + \frac{\rho_0 g}{c_0^2} (z_i - z_k) \right] \tag{14}$$

Apart from the continuity equation, DBPs also take part in the computations of momentum equations. However, their positions are not updated according to the computed acceleration. They either keep stationary on the contour of the numerical wave flume or move with the wavemaker and floating body. The computed acceleration is used to calculate the fluid force exerted by fluid particle  $i$  on DBP  $k$ :

$$f_{i \rightarrow k} = - \sum_i (p_i + p_k) \nabla_k W_{ki} V_i V_k + \mathbf{g} + a h c_0 \rho_0 \sum_i \pi_{ki} \nabla_k W_{ki} V_i V_k \tag{15}$$

By summing up  $f_{i \rightarrow k}$  of all fluid particles in the kernel support, the total fluid force exerted on DBP  $k$  is obtained:

$$f_k = \sum_i f_{i \rightarrow k} \tag{16}$$

Then, the total fluid force acting on the floating body is obtained by summing up  $f_k$  of all DBPs constituting the floating body:

$$F_f = \sum_k f_k = \sum_k \sum_i f_{i \rightarrow k} \tag{17}$$

Correspondingly, the total fluid force moment on the floating body can be calculated by:

$$T_f = \sum_k (\mathbf{r}_k - \mathbf{r}_c) \times f_k = \sum_k \sum_i \left\{ (\mathbf{r}_k - \mathbf{r}_c) \times \sum_i f_{i \rightarrow k} \right\} \tag{18}$$

where  $\mathbf{r}_c$  is the position of the center of mass of the floating body.

### 2.2.2. Mooring System Implementation

The mooring system of the floating body is implemented by using a simplified lumped-mass method [89]. Specifically, as depicted in Figure 2, the mooring line is broken up into  $P$  even-length segments connecting  $P + 1$  nodes. Each segment is regarded as a massless spring and its mass is equally distributed to the adjacent nodes. The static force equilibrium equations at node  $p$  are established as follows:

$$F_{m,p} \cos \theta_p = F_{m,p-1} \cos \theta_{p-1} \tag{19}$$

$$F_{m,p} \sin \theta_p = F_{m,p-1} \sin \theta_{p-1} + \omega l_0 \tag{20}$$

where  $F_{m,p}$  is the mooring force between nodes  $p$  and  $p + 1$ , and  $F_{m,p-1}$  is the mooring force between nodes  $p - 1$  and  $p$ ;  $\theta_p$  is the angle between segment  $p$  and horizontal axis, and  $\theta_{p-1}$  is the angle between segment  $p - 1$  and horizontal axis;  $\omega$  is the wet weight per unit length of the mooring line;  $l_0$  is the initial length of each segment.

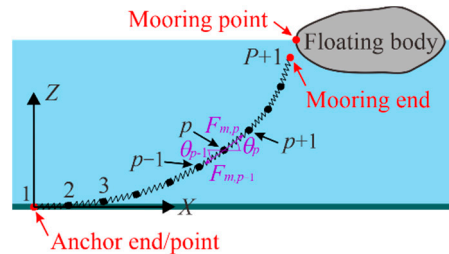


Figure 2. Sketch of the lumped-mass model.

Based on Equations (19) and (20), we have:

$$F_{x,p} = F_{m,p} \cos \theta_p = \dots = F_{m,2} \cos \theta_2 = F_{m,1} \cos \theta_1 \tag{21}$$

$$F_{z,p} = F_{m,p} \sin \theta_p = F_u + \sum_{q=1}^p \omega q l_0 \tag{22}$$

$$F_{m,p} = \sqrt{F_{x,p}^2 + F_{z,p}^2} \tag{23}$$

where  $F_{x,p}$  and  $F_{z,p}$  are the horizontal and vertical mooring force between  $p$  and  $p + 1$ , respectively;  $F_u$  is the uplift force at the anchor point; subscript  $q$  is a counter;  $\omega_q = \omega/2$  when  $q = 1$ , and  $\omega_q = \omega$  when  $2 \leq q \leq p$ . Thus,

$$\cos \theta_p = \frac{F_{x,p}}{F_{m,p}} \tag{24}$$

$$\sin \theta_p = \left( F_u + \sum_{q=1}^p \omega q l_0 \right) / F_{m,p} \tag{25}$$

According to Hooke’s law, the length of the mooring segment after elongation  $l_q$  is:

$$l_p = l_0 \left( 1 + \frac{F_{m,p}}{EA} \right) \tag{26}$$

where  $EA$  is the tensile stiffness of the mooring line. Therefore, the horizontal and vertical positions of the mooring end are calculated by:

$$X_{p+1} = \sum_{p=1}^P (l_p \cos \theta_p) = \sum_{p=1}^P \left[ l_0 \left( 1 + \frac{F_{m,p}}{EA} \right) \frac{F_{x,p}}{F_{m,p}} \right] \tag{27}$$

$$Z_{p+1} = \sum_{p=1}^P (l_p \sin \theta_p) = \sum_{p=1}^P \left[ l_0 \left( 1 + \frac{F_{m,p}}{EA} \right) \left( F_u + \sum_{q=1}^p \omega q l_0 \right) / F_{m,p} \right] \tag{28}$$

The process of solving mooring force is introduced as follows. After computing the motion of the floating body according to Equations (9) and (10),  $Z_{p+1}$  is compared with the vertical position of the mooring point  $z_m$ . When  $Z_{p+1} < z_m$ , nodes of the mooring line are lifted successively from No.  $P + 1$  to No. 2. In case all nodes have been lifted, the uplift force  $F_u$  begins to increase to reduce the slackness of the mooring line, hence further elevating the mooring end. When  $Z_{p+1} > z_m$ ,  $F_u$  decreases, and if  $Z_{p+1}$  is still greater than

$z_m$  when  $F_u = 0$ , nodes fall to the seabed successively from No. 2 to No.  $P + 1$ . Then,  $X_{P+1}$  is compared with the horizontal position of the mooring point  $x_m$ . When  $X_{P+1} < x_m$ , the horizontal mooring force  $F_{x,P+1}$  increases, and when  $X_{P+1} > x_m$ ,  $F_{x,P+1}$  decreases. The above process is repeated until both the error between  $Z_{P+1}$  and  $z_m$  and the error between  $X_{P+1}$  and  $x_m$  are allowable. Finally, the mooring force  $F_{m,P+1}$  is calculated according to Equations (21)–(23).

It should be mentioned that the present lumped-mass model only accounts for the tensile force, gravity and buoyancy of the mooring line, but neglects the hydrodynamic force induced by the wave and current, inertial force due to the variable motion of the mooring line, damping force accompanied by the lengthening and shortening of the mooring line and frictional force caused by the contact between mooring line and seabed, etc. This will certainly affect the computed mooring force and thereby influence the computed hydrodynamic characteristics of the floating body, but will be insufficient to change the research conclusions. Nevertheless, the sophisticated lumped-mass model established by Hall and Goupee [72] is highly recommended. Based on that model, an open-source mooring library MoorDyn was developed and incorporated into DualSPHysics [71], making the SPH simulation of wave-moored floating body advanced and convenient.

### 3. Model Validation

A 2-D numerical wave flume was established where two physical model experiments on waves interaction with the cuboid and dual cylindrical floating pontoons were reproduced. The numerical model was validated by comparing the experimental and numerical wave transmission coefficients, wave reflection coefficients, response amplitude operators of floating pontoons and mooring force.

#### 3.1. Numerical Wave Flume

The numerical wave flume established to simulate the interaction between waves and moored floating bodies is shown in Figure 3. A piston was equipped at the upstream end of the flume, which, based on the active absorption wave-making theory [90], generated target waves while absorbing the reflected waves from the floating body. At the other end, a sponge layer was arranged to eliminate the outgoing waves. In the sponge layer, the momentum equation of fluid particles is rewritten as [50]

$$r_i = \frac{Du_i}{Dt} = -\frac{1}{\rho_i} \sum_j (p_j + p_i) \nabla_i W_{ij} V_j + \mathbf{g} + \alpha h c_0 \frac{\rho_0}{\rho_i} \sum_j \pi_{ij} \nabla_i W_{ij} V_j - \beta \frac{x_i - x_s}{L_s} \mathbf{u}_i \quad (29)$$

where  $x_i$  is the horizontal position of the fluid particle labeled as  $i$ ;  $x_s$  is the horizontal position of the interface between sponge layer and common fluid domain;  $L_s = \lambda$  is the length of the sponge layer with  $\lambda$  being the wavelength;  $\beta$  is the intensity coefficient of the sponge layer, which can be taken from Reference [91]. In this study,  $\beta$  ranges between 0.8 and 5.7 depending on different cases.

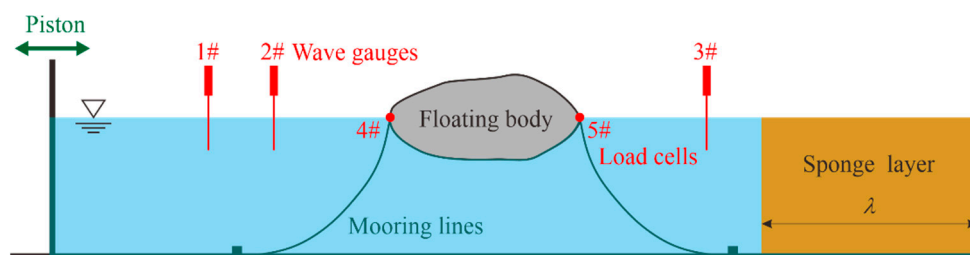


Figure 3. Numerical wave flume used to simulate the interaction between waves and mooring floating bodies.

The floating body was restrained by two mooring lines. #4 and #5 load cells were installed to measure the seaward mooring force  $F_s$  and leeward mooring force  $F_l$ , respectively. On the upstream of the floating body, #1 and #2 wave gauges were arranged, and

the two-point method [92] was used to calculate the reflected wave height  $H_r$ . On the downstream of the floating body, #3 wave gauge was placed. Since high-order wave components generated during the interaction between wave and floating body were weak, the transmitted wave height  $H_t$  was taken as the height difference between the wave crest and wave trough. Thus, the wave reflection coefficient  $C_r$  and the wave transmission coefficient  $C_t$  of the floating body are defined as

$$C_r = \frac{H_r}{H} \quad C_t = \frac{H_t}{H} \tag{30}$$

where  $H$  is the incident wave height. The response amplitude operators of the sway motion  $RAO_s$ , heave motion  $RAO_h$  and roll motion  $RAO_r$  of the floating body are defined as

$$RAO_s = \frac{2A_s}{H} \quad RAO_h = \frac{2A_h}{H} \quad RAO_r = \frac{2A_r}{H} \tag{31}$$

where  $A_s$ ,  $A_h$  and  $A_r$  are the amplitudes of the sway, heave and roll motion of the floating body, respectively. For each wave condition, 30 wave cycles were run and the last 15 wave cycles were taken for analysis. The height and period of the generated wave were checked prior to simulating the interaction between wave and moored floating body.

### 3.2. Validation Case 1

#### 3.2.1. Setup of Physical and Numerical Models

Physical model experiment 1 on waves interaction with a cuboid floating pontoon was carried out at Jiangsu University of Science and Technology [93]. The wave flume is 45 m long, 0.8 m wide and 1.2 m high. At the one end there is a piston-type wavemaker. At the other end an absorbing beach composed of armor blocks, inclined and vertical porous plates is placed. The experiment was designed based on the gravity similarity criterion, and the model to prototype length scale factor was 1:20. The setup of the physical pontoon and its mooring system is shown in Figure 4a, and the parameters are listed in Table 1. Water depth  $d$  was fixed at 1.0 m. Two regular wave heights  $H = 0.10$  m and 0.15 m were adopted, and wave periods  $T$  ranged between 1.0 s and 4.6 s. Two wave gauges for decomposing the incident and reflected waves were placed 5.0 m and 5.4 m upstream from the pontoon. Three wave gauges were placed 4.0 m, 17.0 m and 17.4 m downstream from the pontoon, in which the nearest gauge to the pontoon was used to measure the transmitted waves. The sway, heave and roll motion of the pontoon was captured by using a 6-DOF tracking system. The seaward and leeward mooring force was obtained from the load cells equipped on both sides of the pontoon.

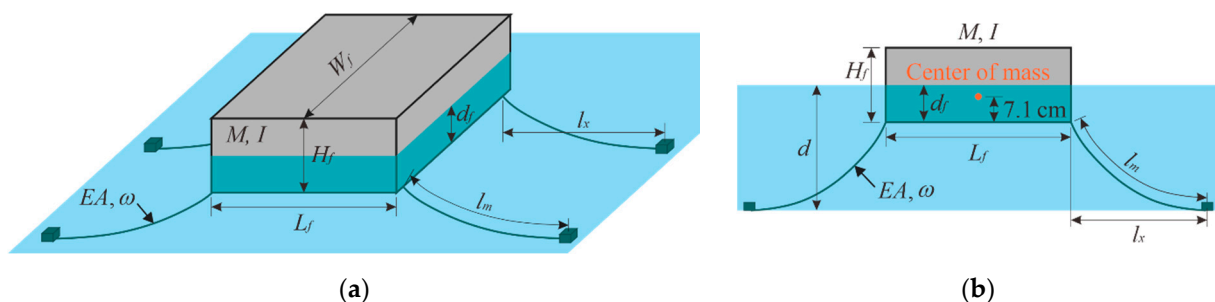


Figure 4. Setup of the cuboid floating pontoon and its mooring system: (a) Physical model; (b) Numerical model.

**Table 1.** Parameters of the cuboid floating pontoon and its mooring system.

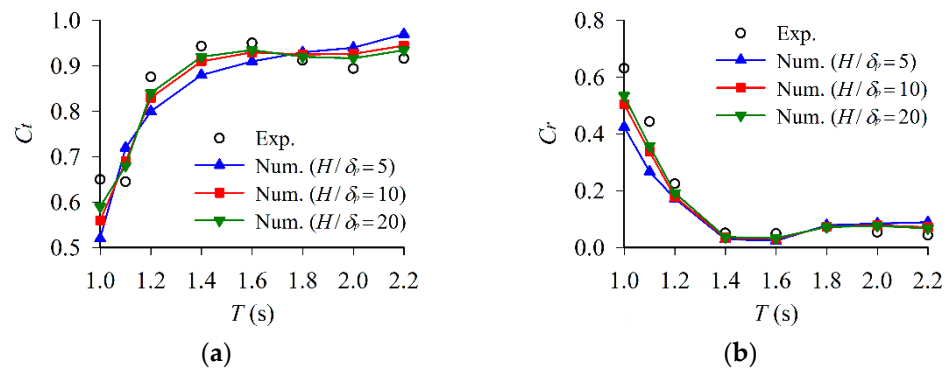
Floating Pontoon	Length $L_f$	Width $W_f$	Height $H_f$	Draft $d_f$	Mass $M$	Moment of Inertia $I$
Exp. values	50 cm	76 cm	20 cm	10 cm	28.6 kg	0.669 kg·m <sup>2</sup>
Num. values	same	100 cm	same	same	$28.6/76 \times 100 = 37.63$ kg	$0.669/76 \times 100 = 0.88$ kg·m <sup>2</sup>
Mooring System	Tensile Stiffness $EA$		Wet Weight $w$		Bending Length $l_m$	Horizontal Length $l_x$
Exp. values	3.15 kN		6.18 N/m		1.6 m	1.15 m
Num. values	$3.15 \times 2/76 \times 100 = 8.29$ kN		$6.18 \times 2/76 \times 100 = 16.26$ N/m		same	same

2-D numerical simulations were performed in the numerical wave flume shown in Figure 3. The numerical pontoon and its mooring system are illustrated in Figure 4b, and their parameters are listed in Table 1. Note that since the physical model is 3D and the numerical model is 2D, the mass  $M$  and moment of inertia  $I$  of the numerical pontoon and the tensile stiffness  $EA$  and wet weight  $w$  of the numerical mooring system were converted. As a validation case, only conventional wave conditions of  $H = 0.10$  m and  $T = 1.0$ – $2.2$  s were reproduced. Three particle resolutions  $H/\delta_p = 5, 10$  and  $20$  (i.e., initial particle spacing  $\delta_p = 2$  cm,  $1$  cm and  $0.5$  cm) were adopted to check the numerical convergence and find the optimal  $\delta_p$ . Under various  $H/\delta_p$  and  $T$ , a total number of 31,380–799,240 particles were used, resulting in runtimes of 0.4–61.9 h on an Intel Core i9-9900X CPU @ 3.50GHz.

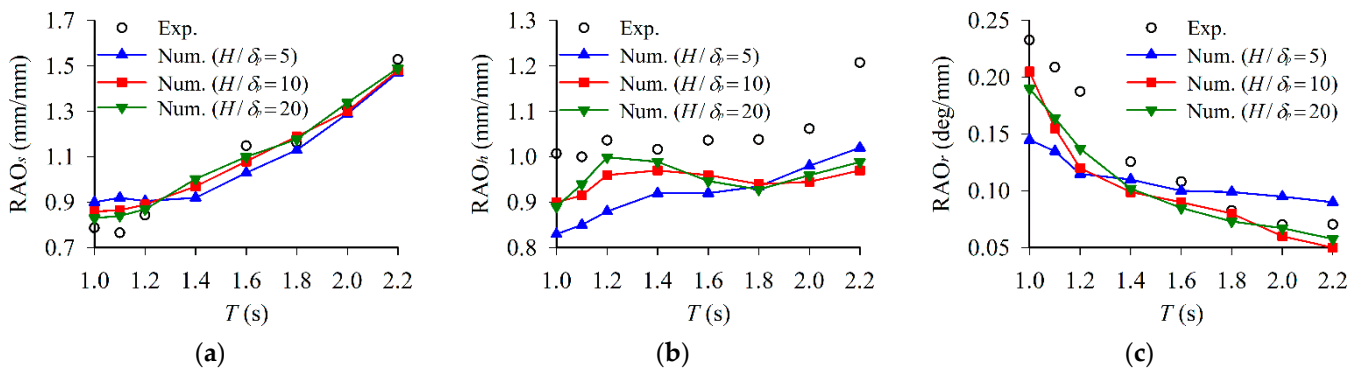
### 3.2.2. Comparison of Experimental and Numerical Results

Figure 5 compares the experimental and numerical wave transmission coefficients  $C_t$  and reflection coefficients  $C_r$  of the cuboid floating pontoon. Regardless of the particle resolution  $H/\delta_p$ , the overall trends are in reasonable agreement. When  $T \leq 1.6$  s, the numerical  $C_t$  and  $C_r$  are generally less than the experimental data. This is related to the dissipation nature of the SPH method [94]. Since the physical and numerical wave gauges used to measure the transmitted and reflected waves are at the same distance from the pontoon, more energies have been dissipated before the numerical wave arrives at the wave gauges. The numerical dissipation decreases with the increment of  $T$ , and when  $T > 1.6$  s the numerical  $C_t$  and  $C_r$  become no longer less but even greater than the experimental data. The greater numerical results might be associated with the absence of turbulence model in the present numerical model. On such premise, energy dissipation caused by the numerical turbulent flow is under-predicted. It can be further observed that both numerical  $C_t$  and  $C_r$  basically converge toward the experimental data with the increase of  $H/\delta_p$ . Doubling  $H/\delta_p$  from 5 to 10 significantly enhances the numerical accuracy, while doubling  $H/\delta_p$  from 10 to 20 has limited effect. Therefore, based on a trade-off between numerical accuracy and computational efficiency,  $H/\delta_p = 10$  is a proper particle resolution in terms of  $C_t$  and  $C_r$  computations. It is worth mentioning that  $H/\delta_p = 10$  is also recommended by Altomare et al. [95] as the threshold of accurately and affordably modelling the wave generation, propagation and absorption.

Figure 6 compares the experimental and numerical response amplitude operators of the sway motion  $RAO_s$ , heave motion  $RAO_h$  and roll motion  $RAO_r$  of the cuboid floating pontoon. Intuitively, the experimental and numerical  $RAO_s$  are in better agreement. Although the experimental and numerical  $RAO_h$  and  $RAO_r$  have the same trends, the numerical results are noticeably less than the experimental data. However, if taking account of the different variation ranges of  $RAO_s$ ,  $RAO_h$  and  $RAO_r$ , the degrees of agreement shown in Figure 6a–c are comparable and all acceptable. According to Equations (9) and (10), the motion of the pontoon is subjected to fluid force and mooring force, which means that the discrepancies in  $RAO_s$ ,  $RAO_h$  and  $RAO_r$  are caused by the computational inaccuracies of fluid force and mooring force.



**Figure 5.** Comparison of the experimental and numerical wave transmission coefficients and reflection coefficients of the cuboid floating pontoon: (a) Wave transmission coefficient  $C_t$ ; (b) Wave reflection coefficient  $C_r$ .



**Figure 6.** Comparison of the experimental and numerical response amplitude operators of the cuboid floating pontoon: (a) Sway motion RAO<sub>s</sub>; (b) Heave motion RAO<sub>h</sub>; (c) Roll motion RAO<sub>r</sub>.

Our previous study on waves interaction with fixed and freely floating bodies [86] demonstrated the reliability of fluid force computation, so it is speculated that the absence of hydrodynamic, inertial, damping and frictional contributions in the present mooring model is responsible for the discrepancies. In addition, the side-wall effect of the physical experiment also brings certain interference in the motion of the pontoon. Regarding particle resolution,  $H/\delta_p = 20$  leads to the favorable numerical results compared with the experimental data.  $H/\delta_p = 10$  yields the second-best numerical results which are sufficiently close to those of  $H/\delta_p = 20$ . Therefore,  $H/\delta_p = 10$  is the optimal particle resolution in terms of RAO<sub>s</sub>, RAO<sub>h</sub> and RAO<sub>r</sub> computations.

Figure 7 compares the experimental and numerical mooring force on the seaward side  $F_s$  and leeward side  $F_l$  of the cuboid floating pontoon. There were two anchor chains on each side of the 76 cm-wide physical pontoon and there was one anchor chain on each side of the 100 cm-wide numerical pontoon. Thus, the computed mooring force was divided by 2 and multiplied by 0.76 before being compared with the experimental data. From Figure 7, it can be seen that the numerical  $F_s$  and  $F_l$  follow the same trends as the experimental data, but the numerical results are generally over-predicted. Although the discrepancies seem significant, the relative errors ( $RE = |\text{numerical value} - \text{experimental value}| / \text{experimental value}$ ) are small. Under  $H/\delta_p = 5$ , the average REs of  $F_s$  and  $F_l$  are 8.0% and 5.5%, respectively. Under  $H/\delta_p = 10$ , the average REs of  $F_s$  and  $F_l$  decrease to 6.3% and 4.1%, respectively. Under  $H/\delta_p = 20$ , the average REs of  $F_s$  and  $F_l$  are as small as 5.1% and 3.4%, respectively. The two aforementioned facts could have accounted for the discrepancies in the mooring force. First, the side-wall effect of the physical experiment slightly interferes with the motion of the pontoon. It is known that the mooring force is largely dependent on the mooring position. Thus, the disturbed motion of the physical pontoon lowers the degree of

agreement between the experimental and numerical mooring force. Second, the present mooring model neglects the hydrodynamic, inertial, damping and frictional contributions. As documented by Hall et al. [96] and Davidson and Ringwood [97], the mooring dynamics are quite different, incorporating or not incorporating these contributions.

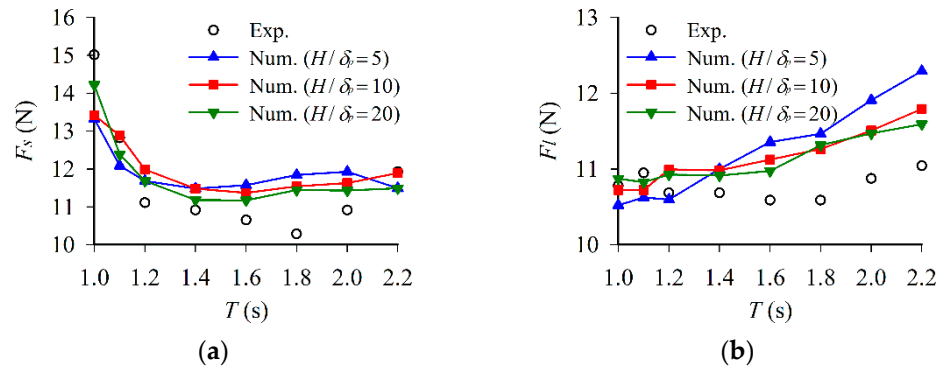


**Figure 7.** Comparison of the experimental and numerical mooring force of the cuboid floating pontoon: (a) Seaward side  $F_s$ ; (b) Leeward side  $F_l$ .

3.3. Validation Case 2

3.3.1. Setup of Physical and Numerical Models

Physical model experiment 2 on waves interaction with a dual cylindrical floating pontoon was conducted in the same flume at Jiangsu University of Science and Technology [93]. The physical pontoon and its mooring system are illustrated in Figure 8a, and the parameters of the pontoon are listed in Table 2. Except for the pontoon, all the other setup, including the mooring system, wave conditions and measurement instruments, were consistent with those in the physical model experiment 1.

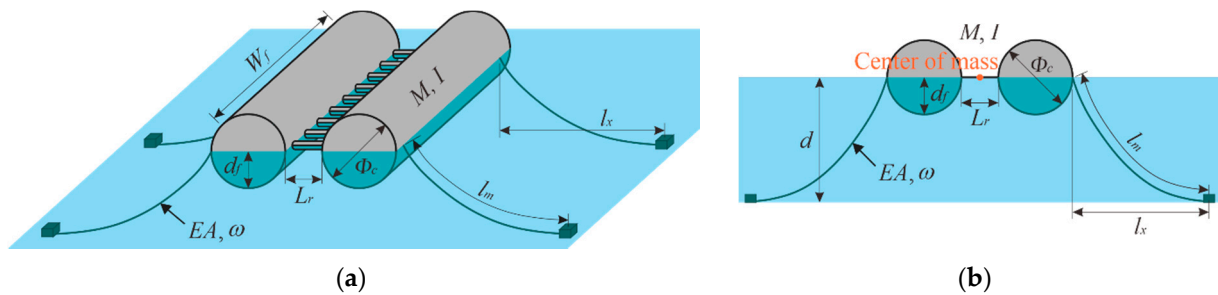


**Figure 8.** Setup of the dual cylindrical floating pontoon and its mooring system: (a) Physical model; (b) Numerical model.

**Table 2.** Parameters of the dual cylindrical floating pontoon.

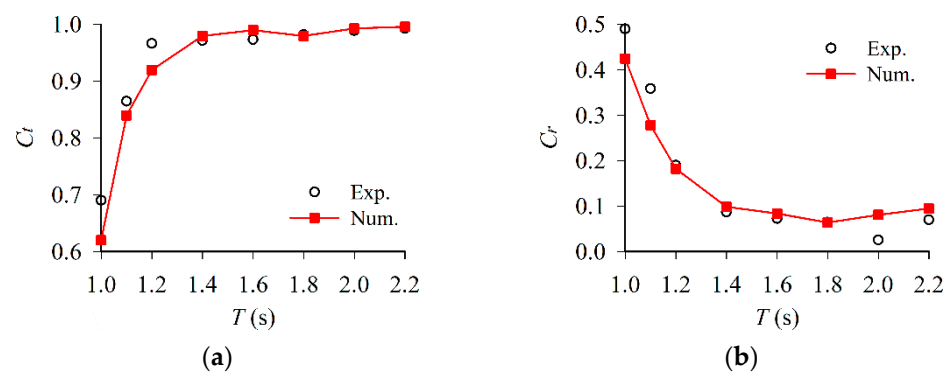
Floating Pontoon	Diameter $F_c$	Width $W_f$	Interspacing $L_r$	Draft $d_f$	Total Mass $M$	Total Moment of Inertia $I$
Exp. values	20 cm	76 cm	10 cm	10 cm	19.1 kg	0.474 kg·m <sup>2</sup>
Num. values	same	100 cm	same	same	$19.1/76 \times 100 = 25.14$ kg	$0.474/76 \times 100 = 0.624$ kg·m <sup>2</sup>

2-D numerical simulations were also performed in the numerical wave flume shown in Figure 3. The setup of the numerical pontoon and its mooring system is shown in Figure 8, and the parameters of the pontoon are listed in Table 2. Again, wave height  $H$  was fixed at 0.10 m and the wave period ranged between 1.0 s and 2.2 s. According to the convergence analysis made in Section 3.2, particle resolution was taken as  $H/\delta_p = 10$

(i.e.,  $\delta_p = 1$  cm), thus requiring 125,232–199,304 particles in the simulations and resulting in runtimes of 2.8–6.2 h.

### 3.3.2. Comparison of Experimental and Numerical Results

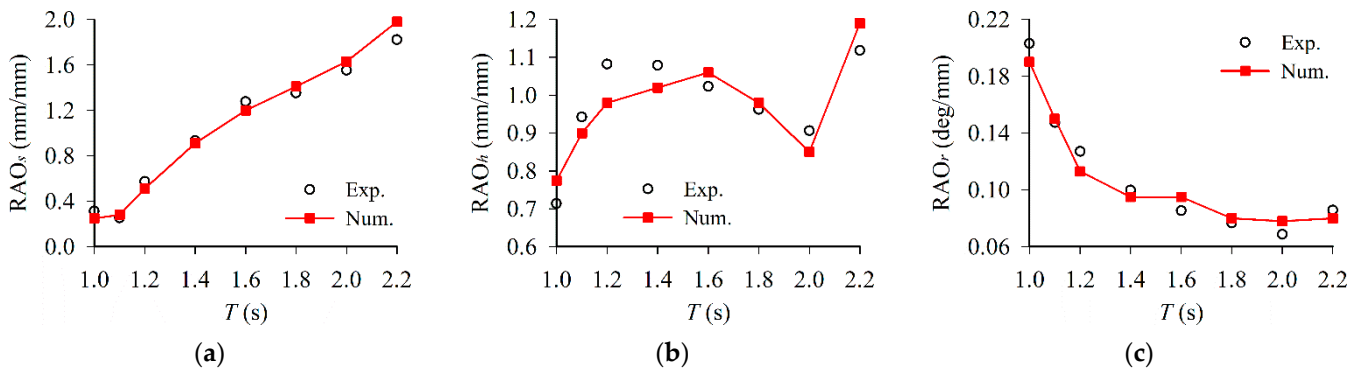
Figure 9 compares the experimental and numerical  $C_t$  and  $C_r$  of the dual cylindrical floating pontoon. Again, the overall agreement is satisfactory. In Figure 9a, when  $T \leq 1.2$  s the numerical  $C_t$  are less than the experimental data, and when  $T > 1.2$  s the numerical  $C_t$  are greater. This discrepancy has been explained in Section 3.2.2 as the comprehensive result of the dissipation nature of the SPH method and the absence of turbulence model in the present numerical model. It is worth noticing that in Figure 9a the threshold value (less than which the numerical results are under-predicted while greater than which the numerical results are over-predicted) of  $T$  is 1.2 s which is less than the 1.6 s in Figure 5a. This is probably because the 2-D numerical model abandons the nine connecting rods of the 3-D physical model. Thus, the turbulent energy dissipation in the process of flow passing through the rods is neglected in the simulation, resulting in over-predicted numerical  $C_t$ . Unlike the transmitted wave, the reflected wave mainly depends on the frontal area and structural shape of the floating breakwater. Thus, abandoning the physical rods makes little difference on the numerical  $C_r$ . The manifestation is that the numerical  $C_r$  in Figure 9b has the same threshold value of  $T$ , namely 1.6 s, as Figure 5b.



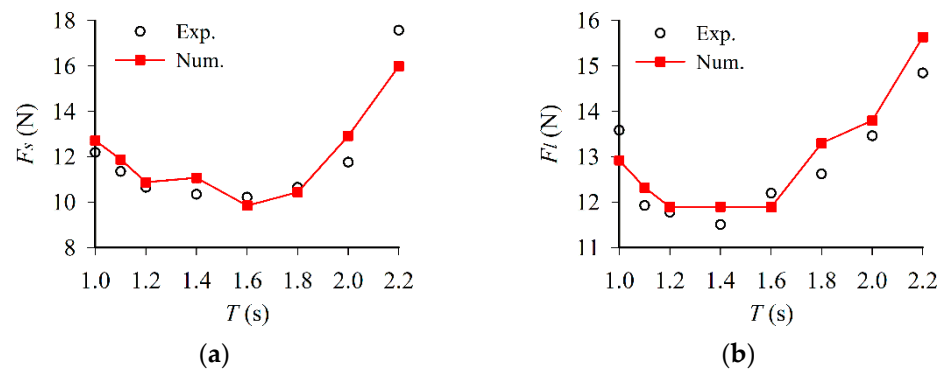
**Figure 9.** Comparison of the experimental and numerical wave transmission coefficients and reflection coefficients of the dual cylindrical floating pontoon: (a) Wave transmission coefficient  $C_t$ ; (b) Wave reflection coefficient  $C_r$ .

Figure 10 compares the experimental and numerical  $RAO_s$ ,  $RAO_h$  and  $RAO_r$  of the dual cylindrical floating pontoon. For  $RAO_s$  and  $RAO_r$ , the maximum relative errors REs are 19.9% and 13.7%, which occur at  $T = 1.0$  s and 2.0 s, respectively. These two REs are remarkable just because the experimental data, as denominators, are small. However, the average REs of  $RAO_s$  and  $RAO_r$  within the entire  $T$  range are only 8.6% and 7.5%, respectively. As for  $RAO_h$ ,  $T = 1.2$  s corresponds to the maximum RE equaling 9.4%, and the average RE is 5.8%. In view of the insignificant average REs, the  $RAO_s$ ,  $RAO_h$  and  $RAO_r$  computations regarding the cylindrical floating pontoon are reliable.

Figure 11 compares the experimental and numerical  $F_s$  and  $F_l$  of the dual cylindrical floating pontoon. Owing to the side-wall effect of the physical experiment and the lack of hydrodynamic, inertial, damping and frictional contributions in the numerical mooring model, discrepancies between experimental and numerical  $F_s$  and  $F_l$  can be observed. The degrees of deviation are comparable with those in Figure 7, and quantitatively, the average REs of  $F_s$  and  $F_l$  are merely 5.4% and 3.6%, respectively. Therefore, the mooring force computation regarding the cylindrical floating pontoon is also reliable.



**Figure 10.** Comparison of the experimental and numerical response amplitude operators of the dual cylindrical floating pontoon: (a) Sway motion  $RAO_s$ ; (b) Heave motion  $RAO_h$ ; (c) Roll motion  $RAO_r$ .



**Figure 11.** Comparison of the experimental and numerical mooring force of the dual cylindrical floating pontoon: (a) Seaward side  $F_s$ ; (b) Leeward side  $F_l$ .

#### 4. Results and Analyses

The validated numerical model was applied to study the influence of separation distance and wave parameters on the wave transmission coefficient, response amplitude operators and mooring force of a prototype double-row floating breakwater composed of a cuboid pontoon and a cylindrical airbag.

##### 4.1. Setup of Double-Row Floating Breakwater

Simulations were performed in the numerical wave flume shown in Figure 12. A cuboid pontoon and a cylindrical airbag with separation distance  $s$  were arranged. The length  $L_f$ , height  $H_f$ , draft  $d_{f1}$ , mass  $M_1$  and moment of inertia  $I_1$  of the pontoon were 10 m, 2.5 m, 1.5 m, 15 t, and  $136.56 \text{ t}\cdot\text{m}^2$ , respectively, and the height of the center of mass  $c_{m1}$  was 0.75 m. The diameter  $\Phi_c$ , draft  $d_{f2}$ , mass  $M_2$  and moment of inertia  $I_2$  of the airbag were 5 m, 4 m, 1.5 m, 16.84 t and  $76.93 \text{ t}\cdot\text{m}^2$ , respectively, and the height of the center of mass  $c_{m2}$  was 2.18 m. Both pontoon and airbag were restrained by two mooring lines with mooring angle  $\theta = 30^\circ$ , tensile stiffness  $EA = 2.76 \text{ MN}$  and wet weight  $w = 0.19 \text{ kN/m}$ . For pontoon, mooring points located at its upper corners. The bending length of the mooring line  $l_{m1}$  was 78.67 m and the horizontal distance between mooring point and anchoring point  $l_{x1}$  was 74.56 m. 2# and 3# load cells were installed to measure the seaward mooring force  $F_{s1}$  and leeward mooring force  $F_{l1}$ , respectively. For airbag, mooring points located at its outermost tips, the bending length of the mooring line  $l_{m2}$  was 69.04 m and the horizontal distance between mooring point and anchoring point  $l_{x2}$  was 65.69 m. 4# and 5# load cells were installed to measure the seaward mooring force  $F_{s2}$  and leeward mooring force  $F_{l2}$ , respectively. 1# wave gauge was placed  $0.75\lambda$  downstream from the airbag to obtain the wave transmission coefficient  $C_t$ .  $s$  varied between  $\lambda/4$  and  $\lambda$  with an interval of  $\lambda/4$ . Water depth  $d$  was fixed at 20 m. Regular waves of four heights,  $H = 1 \text{ m}, 2 \text{ m}, 3 \text{ m}$  and  $4 \text{ m}$ ,

and four periods,  $T = 4\text{ s}$ ,  $5\text{ s}$ ,  $6\text{ s}$  and  $7\text{ s}$ , were tested. Since  $H/\delta_p = 10$  has been shown to be suitable regarding numerical accuracy and computational efficiency,  $\delta_p = 10\text{ cm}$  was taken to handle the minimum wave height  $H = 1\text{ m}$ . Thus, a total numerical of 204,810–641,780 particles were deployed depending on different  $T$  and  $s$ , and it took 6.3–42.6 h to simulate 30 wave cycles.

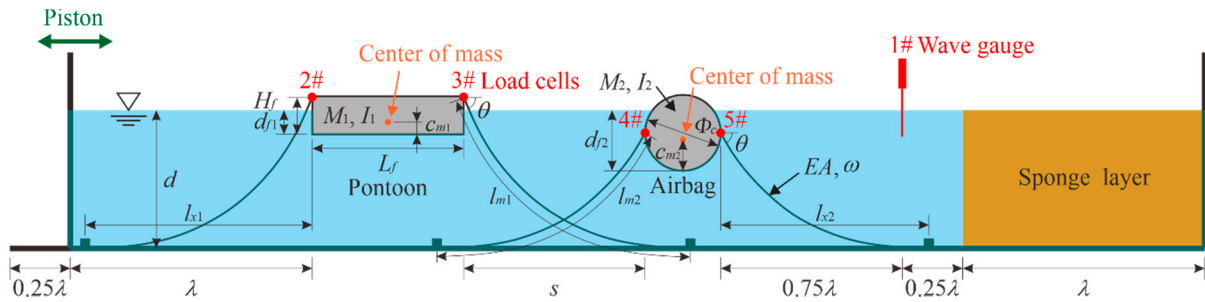


**Figure 12.** Numerical wave flume used to simulate the interaction between waves and a pontoon-airbag double-row floating breakwater.

#### 4.2. Influence of Separation Distance

Taking two wave conditions,  $H = 2\text{ m}$ ,  $T = 4\text{ s}$  and  $H = 2\text{ m}$ ,  $T = 6\text{ s}$ , as examples, Figure 13 shows the wave transmission coefficients  $C_t$  of the double-row floating breakwater with different separation distance  $s/\lambda$ . Meanwhile, the results are compared with  $C_t$  of a single pontoon which is identical to the one used in the double-row floating breakwater. When  $T = 4\text{ s}$ , the average  $C_t$  of the pontoon-airbag system is 0.03 less than  $C_t$  of the single pontoon, and when  $T = 6\text{ s}$ , the average  $C_t$  of the pontoon-airbag system is 0.14 less than  $C_t$  of the single pontoon. It indicates that adding an airbag on the leeward side of the floating pontoon helps to improve the wave attenuation performance, and the improvement effect is more significant in a long-wave regime. In addition,  $C_t$  of the pontoon-airbag system decreases with increasing  $s/\lambda$  and turns to increase after  $s/\lambda > 0.75$ . Thus,  $s/\lambda = 0.75$  is the optimal separation distance of the pontoon-airbag double-row floating breakwater in terms of wave attenuation performance.

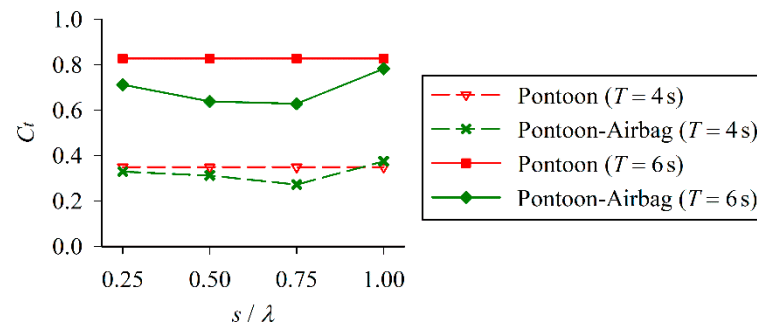


**Figure 13.** Comparison of the wave transmission coefficients  $C_t$  of the double-row floating breakwater with different separation distance  $s/\lambda$ .

Figure 14 presents the response amplitude operators of the sway motion  $RAO_s$ , heave motion  $RAO_h$  and roll motion  $RAO_r$  of the double-row floating breakwater with different separation distance  $s/\lambda$ . It is known that the wave surface measured at 1# wave gauge in Figure 12 is comprised of the transmitted wave after the incident wave passes through the pontoon-airbag system and the radiated wave generated by the motion of the pontoon-airbag system. Thus, the wave height on the leeward side of the pontoon-airbag system is usually positively correlated with the motion amplitudes of the pontoon and airbag, and the variation trends of  $RAO_s$ ,  $RAO_h$  and  $RAO_r$  with  $s/\lambda$  in Figure 14 are consistent

with the variation trend of  $C_t$  in Figure 13. That is,  $RAO_s$ ,  $RAO_h$  and  $RAO_r$  of pontoon and airbag decrease with increasing  $s/\lambda$  and turn to increase after  $s/\lambda > 0.75$ .

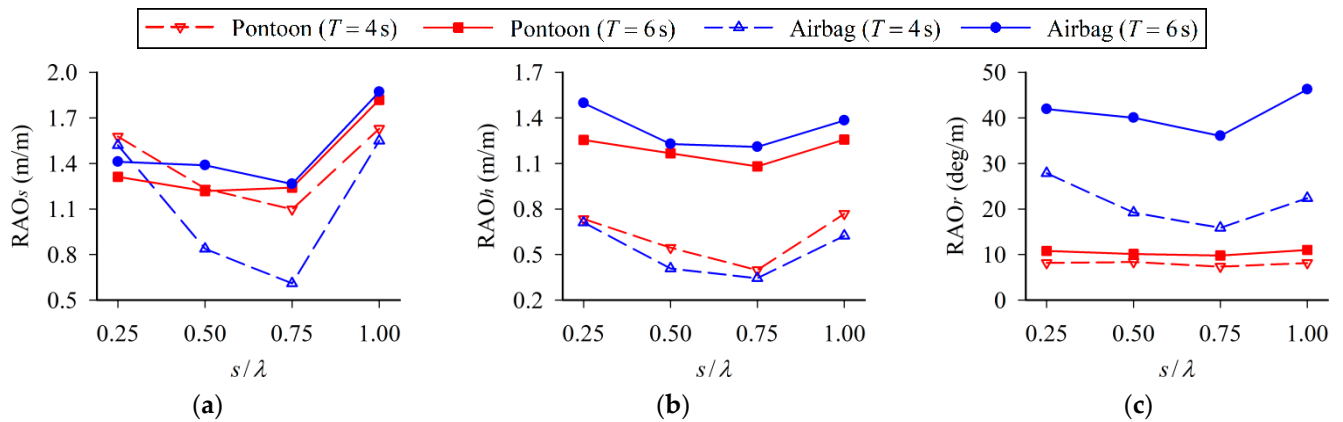


**Figure 14.** Comparison of the response amplitude operators of the double-row floating breakwater with different separation distance  $s/\lambda$ : (a) Sway motion  $RAO_s$ ; (b) Heave motion  $RAO_h$ ; (c) Roll motion  $RAO_r$ .

Figure 15 gives the mooring force on the seaward side  $F_s$  and leeward side  $F_l$  of the double-row floating breakwater with different separation distance  $s/\lambda$ . As mooring force is predominantly dependent on mooring position,  $F_s$  and  $F_l$  in Figure 15 follow the same variation trends as  $RAO_s$ ,  $RAO_h$  and  $RAO_r$  in Figure 14. The minimum  $F_s$  and  $F_l$  are obtained when  $s/\lambda = 0.75$ . However, the maximum  $F_s$  and  $F_l$  occur when  $s/\lambda = 0.25$ , which is different from the result that the maximum  $RAO_s$ ,  $RAO_h$  and  $RAO_r$  appear when  $s/\lambda = 1.00$ . In addition, under both wave periods,  $F_s$  and  $F_l$  of the airbag are greater than those of the pontoon. This phenomenon is consistent with Figure 14c where  $RAO_r$  of the airbag is greater than that of the pontoon, but is different from Figure 14a,b where  $RAO_s$  and  $RAO_h$  of the airbag are less than those of the pontoon. This implies the roll motion of the floating body has the greatest influence on the mooring force.

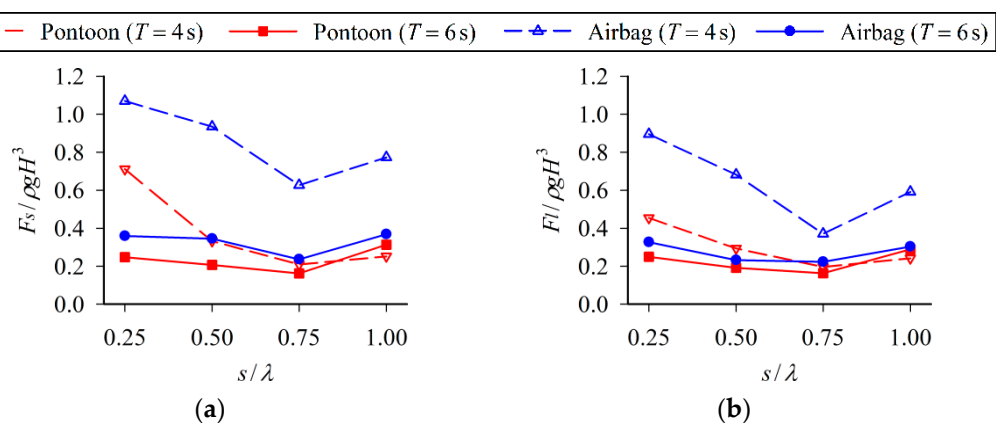
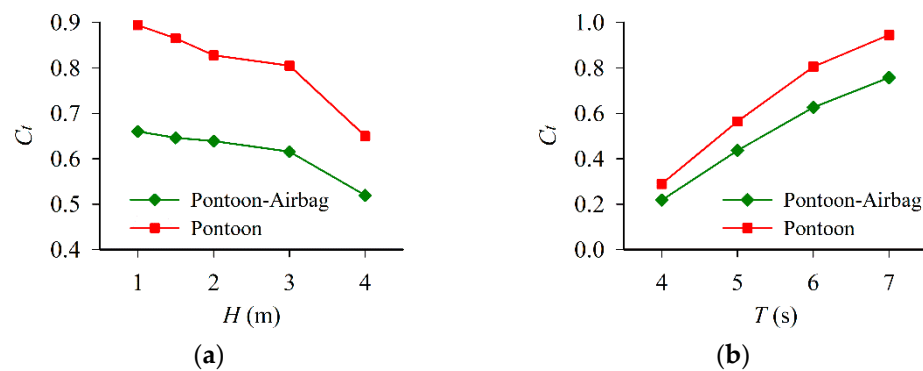


**Figure 15.** Comparison of the mooring force of the double-row floating breakwater with different separation distance  $s/\lambda$ : (a) Seaward side  $F_s$ ; (b) Leeward side  $F_l$ .

### 4.3. Influence of Wave Parameters

Section 4.2 has shown that the optimal separation distance between pontoon and airbag is 0.75 times the wavelength. On this premise, waves interaction with double-row floating breakwater under wave heights  $H = 1-4$  m and wave periods  $T = 4-7$  s are further simulated. The computed  $C_t$  are plotted in Figure 16, and they are compared with  $C_t$  of a single pontoon when the leeward airbag is absent. In Figure 16a,  $C_t$  of both pontoon-airbag system and single pontoon decrease with the increase of  $H$ . The reason may be that as  $H$

increases, the interaction between wave and floating body is intensified; thereby, the wave energy loss due to fluid viscosity becomes heavier. In Figure 16b,  $C_t$  of both pontoon-airbag system and single pontoon increase with the increase of  $T$ , apparently because longer waves have stronger transmission capacity. In fact, the above laws hold for most species of floating breakwaters. Within the concerned wave conditions, the pontoon-airbag system has less  $C_t$  than the single pontoon, i.e., presenting better wave attenuation performance. For one thing, the improvement weakens as  $H$  increases. When  $H = 1$  m, 1.5 m, 2 m, 3 m and 4 m,  $C_t$  of the pontoon-airbag system are 0.23, 0.22, 0.19, 0.19 and 0.13 less than  $C_t$  of the single pontoon, respectively. For another, the improvement strengthens as  $T$  increases. When  $T = 4$  s, 5 s, 6 s and 7 s,  $C_t$  of the pontoon-airbag system are 0.07, 0.13, 0.18 and 0.19 less than  $C_t$  of the single pontoon, respectively.



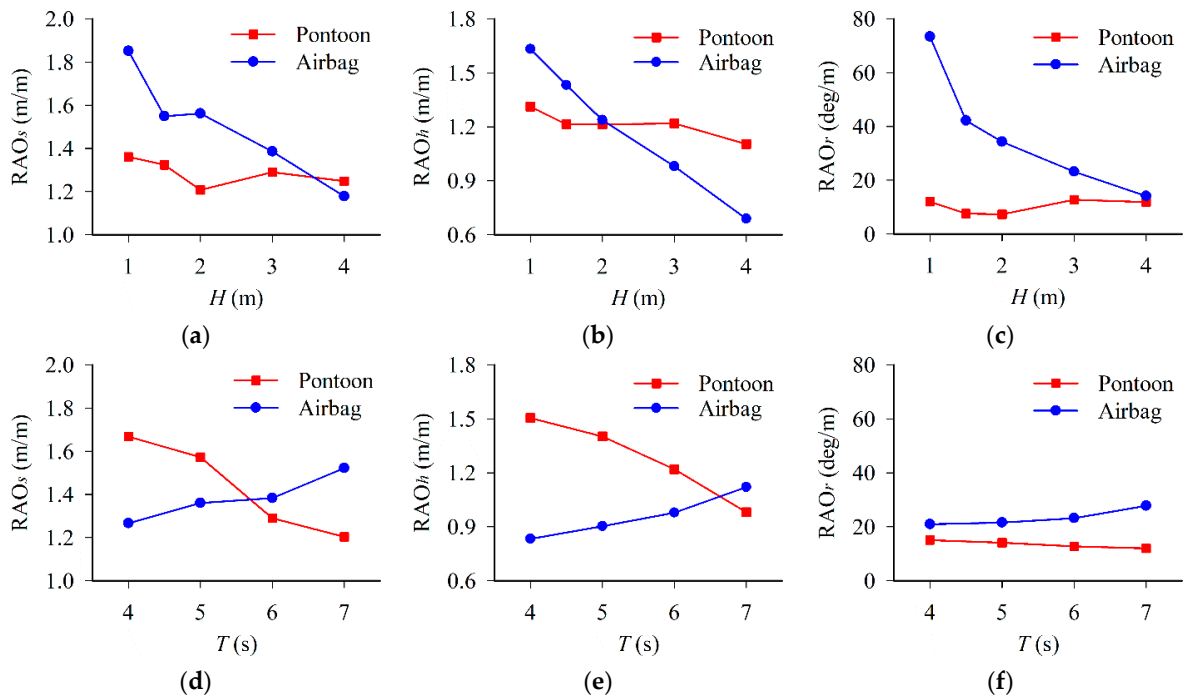
**Figure 16.** Comparison of the wave transmission coefficients  $C_t$  of the double-row floating breakwater under different wave parameters: (a) Wave height  $H = 1\text{--}4$  m and wave period  $T = 6$  s; (b) Wave height  $H = 3$  m and wave period  $T = 4\text{--}7$  s.

Figure 17 shows  $RAO_s$ ,  $RAO_h$  and  $RAO_r$  of the double-row floating breakwater under different  $H$  and  $T$ . From Figure 17a–c, it can be seen that  $H$  has limited influence on  $RAO_s$ ,  $RAO_h$  and  $RAO_r$  of the pontoon. As for the airbag, since more wave energy is dissipated during the wave-pontoon interaction with the increase of  $H$ , the intensity of the leeward wave field is relatively weakened, leading to the rapid decreases in  $RAO_s$ ,  $RAO_h$  and  $RAO_r$  of the airbag. These two trends yield that, when  $H$  is relatively small, the motion amplitudes of the airbag are greater than those of the pontoon, while when  $H$  is relatively large, the motion amplitudes of the pontoon become greater. For  $RAO_s$ ,  $RAO_h$  and  $RAO_r$ , the threshold values of  $H$  are 3.6 m, 2.1 m and 4 m, respectively.

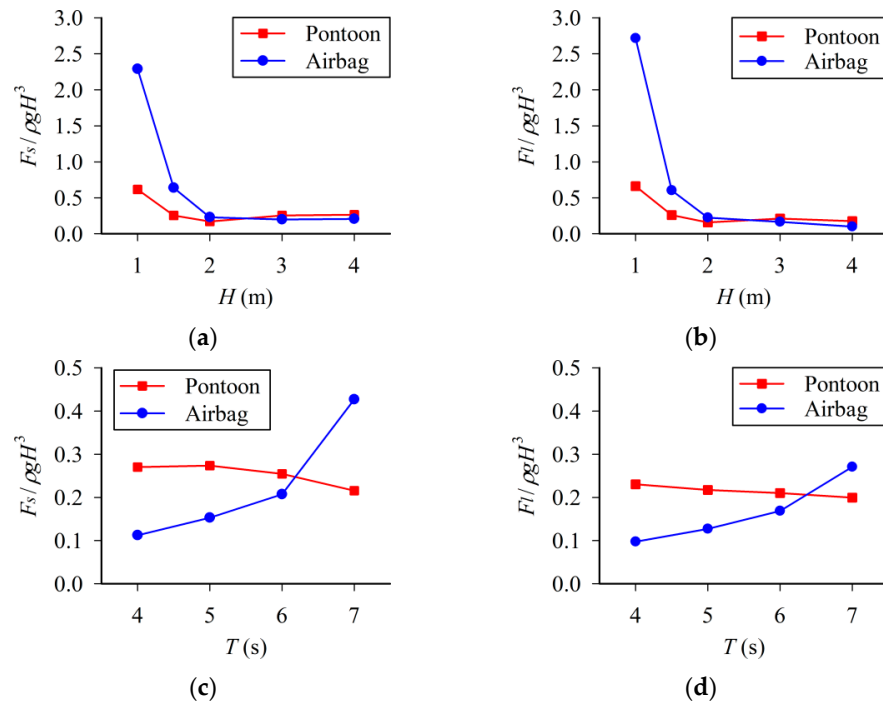
In Figure 17d–f,  $RAO_s$ ,  $RAO_h$  and  $RAO_r$  of the pontoon decrease with the increase of  $T$ , while  $RAO_s$ ,  $RAO_h$  and  $RAO_r$  of the airbag increase with the increase of  $T$ . This is evidently because shorter waves have weaker transmission capacity; thus, the wave energy mainly acts on the seaward pontoon, leading to the greater motion amplitudes of pontoon than an airbag. The wave transmission capacity grows with  $T$ ; thus, more wave energy acts on the leeward airbag, resulting the greater motion amplitudes of the airbag than pontoon. For  $RAO_s$  and  $RAO_h$ , the threshold values of  $T$  are 5.7 and 6.8 s, respectively. However, within the entire  $T$  range,  $RAO_r$  of the airbag is always greater than that of the pontoon, because the moment of inertia of the airbag,  $I_2 = 76.93 \text{ t}\cdot\text{m}^2$ , is much smaller than that of the pontoon,  $I_1 = 136.56 \text{ t}\cdot\text{m}^2$ .

Figure 18 presents  $F_s$  and  $F_l$  of the double-row floating breakwater under different  $H$  and  $T$ . Since mooring force is closely related to mooring position,  $F_s$  and  $F_l$  in Figure 18 follow the same variation trends as  $RAO_s$ ,  $RAO_h$  and  $RAO_r$  in Figure 17. That is, under a given  $T$ ,  $F_s$  and  $F_l$  of both pontoon and airbag decrease with the increase of  $H$ , and  $F_s$  and  $F_l$  of the airbag decrease more rapidly. Under a given  $H$ ,  $F_s$  and  $F_l$  of the pontoon decrease with the increase of  $T$ , while  $F_s$  and  $F_l$  of the airbag increase with the increase of  $T$ . In addition, when  $H \leq 2.6$  m,  $F_s$  and  $F_l$  of the airbag are greater than those of the pontoon, and when  $H > 2.6$  m,  $F_s$  and  $F_l$  of the pontoon turn to be greater. When  $T \leq 6.2$  s,  $F_s$  and

$F_l$  of the pontoon are greater than those of the airbag, and when  $T > 6.2$  s,  $F_s$  and  $F_l$  of the airbag become greater.



**Figure 17.** Comparison of the response amplitude operators of the double-row floating breakwater under different wave parameters: (a) Sway motion  $RAO_s$ ,  $H = 1-4$  m and  $T = 6$  s; (b) Heave motion  $RAO_h$ ,  $H = 1-4$  m and  $T = 6$  s; (c) Roll motion  $RAO_r$ ,  $H = 1-4$  m,  $T = 6$  s; (d) Sway motion  $RAO_s$ ,  $H = 3$  m,  $T = 4-7$  s; (e) Heave motion  $RAO_h$ ,  $H = 3$  m,  $T = 4-7$  s; (f) Roll motion  $RAO_r$ ,  $H = 3$  m,  $T = 4-7$  s.



**Figure 18.** Comparison of the mooring force of the double-row floating breakwater under different wave parameters: (a) Seaward side  $F_s$ ,  $H = 1-4$  m and  $T = 6$  s; (b) Leeward side  $F_l$ ,  $H = 1-4$  m and  $T = 6$  s; (c) Seaward side  $F_s$ ,  $H = 3$  m and  $T = 4-7$  s; (d) Leeward side  $F_l$ ,  $H = 3$  m and  $T = 4-7$  s.

## 5. Conclusions and Future Perspectives

A smoothed particle hydrodynamics (SPH) model was established to simulate the interaction between waves and mooring floating bodies. After being validated by reproducing two physical model experiments, it was used to study the hydrodynamic characteristics of a prototype double-row floating breakwater composed of a cuboid pontoon and a cylindrical airbag. Conclusions are summarized as follows:

- (1) The wave transmission coefficient, response amplitude operators and mooring force of the double-row floating breakwater first decrease then increase with the increase of the separation distance between pontoon and airbag. The optimal separation distance is 0.75 times the wavelength.
- (2) At the optimal separation distance and within the concerned 1–4 m wave heights and 4–7 s wave periods, the pontoon-airbag system presents better wave attenuation performance than a single pontoon. This improvement weakens as wave height increases while strengthens as the wave period increases.
- (3) The wave transmission coefficient, response amplitude operators and mooring force of the double-row floating breakwater all decrease with the increase of incident wave height, which indicates its potential application in a high-wave regime.
- (4) The wave transmission coefficient of the pontoon-airbag system, the response amplitude operators and mooring force of the airbag increase with the increase of incident wavelength, while the response amplitude operators and mooring force of the pontoon decrease.

Despite the achievements reached in this study, the following aspects are worth investigating in the future:

- (1) The airbag was temporarily assumed to be rigid and its mass distribution did not change with the airbag motion. To reflect its physical behavior more realistically, the external flexibility and the internal ballast water should be taken into account.
- (2) No turbulence model was adopted in the fluid equations, and the lumped-mass mooring model neglected the hydrodynamic, inertial, damping, and frictional contributions. To compute the hydrodynamic characteristics of floating breakwater more accurately, a suitable turbulence model and a sophisticated mooring model should be employed.
- (3) Only the influence of separation distance and wave parameters on the hydrodynamic characteristics of double-row floating breakwater was analyzed. To design the floating breakwater more systematically, a parametric study of the pontoon and airbag should be conducted.

**Author Contributions:** Conceptualization, X.C.; methodology, X.C. and M.H.; software, M.H.; validation, M.H. and Q.Z.; formal analysis, X.C. and C.L.; investigation, X.C. and C.L.; resources, X.C. and X.G.; data curation, C.L.; writing—original draft preparation, X.C.; writing—review and editing, M.H. and Q.Z.; visualization, X.C. and Q.Z.; supervision, X.G.; project administration, X.G.; funding acquisition, X.C. and M.H. All authors have read and agreed to the published version of the manuscript.

**Funding:** This research was funded by the National Natural Science Foundation of China, grant number 51709201, and the Natural Science Foundation of the Jiangsu Higher Education Institutions of China, grant number 20KJB416006.

**Institutional Review Board Statement:** Not applicable.

**Informed Consent Statement:** Not applicable.

**Data Availability Statement:** Not applicable.

**Acknowledgments:** The authors are grateful to three anonymous reviewers for their careful reviews and insightful suggestions that have greatly improved the quality of this work.

**Conflicts of Interest:** The authors declare no conflict of interest.

## References

1. Dai, J.; Wang, C.M.; Utsunomiya, T.; Duan, W. Review of recent research and developments on floating breakwaters. *Ocean Eng.* **2018**, *158*, 132–151. [[CrossRef](#)]
2. Mei, C.C.; Black, J.L. Scattering of surface waves by rectangular obstacles in waters of finite depth. *J. Fluid Mech.* **1969**, *38*, 499–511. [[CrossRef](#)]
3. Delavari, E.; Gharabaghi, A.R.M. Simulating regular wave effects on a pile-moored floating breakwater using a modified WCSPH method. *J. Waterw. Port Coast. Ocean Eng.* **2017**, *143*, 04017021. [[CrossRef](#)]
4. Gesraha, M.R. Analysis of PI shaped floating breakwater in oblique waves: I. Impervious rigid wave boards. *Appl. Ocean Res.* **2006**, *28*, 327–338. [[CrossRef](#)]
5. Koraim, A.S.; Rageh, O.S. Effect of under connected plates on the hydrodynamic efficiency of the floating breakwater. *China Ocean Eng.* **2014**, *28*, 349–362. [[CrossRef](#)]
6. Koo, W. Nonlinear time-domain analysis of motion-restrained pneumatic floating breakwater. *Ocean Eng.* **2009**, *36*, 723–731. [[CrossRef](#)]
7. He, F.; Huang, Z.; Law, A.W.-K. Hydrodynamic performance of a rectangular floating breakwater with and without pneumatic chambers: An experimental study. *Ocean Eng.* **2012**, *51*, 16–27. [[CrossRef](#)]
8. Wang, H.Y.; Sun, Z.C. Experimental study of a porous floating breakwater. *Ocean Eng.* **2010**, *37*, 520–527. [[CrossRef](#)]
9. Mani, J.S. Design of Y-frame floating breakwater. *J. Waterw. Port Coast. Ocean Eng.* **1991**, *117*, 105–119. [[CrossRef](#)]
10. Nasri, B.; Moghim, M.N.; Badri, M.A. Experimental study on trapezoidal pontoon-type floating breakwaters with attached porous plates. *J. Ocean Eng. Mar. Energy* **2021**, *7*, 41–57. [[CrossRef](#)]
11. Dong, G.H.; Zheng, Y.N.; Li, Y.C.; Teng, B.; Guan, C.T.; Lin, D.F. Experiments on wave transmission coefficients of floating breakwaters. *Ocean Eng.* **2008**, *35*, 931–938. [[CrossRef](#)]
12. Williams, A.N.; Abul-Azm, A.G. Dual pontoon floating breakwater. *Ocean Eng.* **1997**, *24*, 465–478. [[CrossRef](#)]
13. Ji, C.-Y.; Chen, X.; Cui, J.; Gaidai, O.; Incecik, A. Experimental study on configuration optimization of floating breakwaters. *Ocean Eng.* **2016**, *117*, 302–310. [[CrossRef](#)]
14. Ji, C.; Cheng, Y.; Yang, K.; Oleg, G. Numerical and experimental investigation of hydrodynamic performance of a cylindrical dual pontoon-net floating breakwater. *Coast. Eng.* **2017**, *129*, 1–16. [[CrossRef](#)]
15. Syed, S.A.; Mani, J.S. Performance of rigidly interconnected multiple floating pontoons. *J. Nav. Arch. Mar. Eng.* **2004**, *1*, 3–17. [[CrossRef](#)]
16. Williams, A.N.; Lee, H.S.; Huang, Z. Floating pontoon breakwaters. *Ocean Eng.* **2000**, *27*, 221–240. [[CrossRef](#)]
17. Ji, C.; Deng, X.; Cheng, Y. An experimental study of double-row floating breakwaters. *J. Mar. Sci. Technol.* **2019**, *24*, 359–371. [[CrossRef](#)]
18. Ji, C.-Y.; Zheng, R.-S.; Cui, J.; Wang, Z.-L. Experimental evaluation of wave transmission and dynamics of double-row floating breakwaters. *J. Waterw. Port Coast. Ocean Eng.* **2019**, *145*, 04019013. [[CrossRef](#)]
19. Duan, W.; Xu, S.; Xu, Q.; Ertekin, R.C.; Ma, S. Performance of an F-type floating breakwater: A numerical and experimental study. *Proc. Inst. Mech. Eng. Part M-J. Eng. Marit. Environ.* **2017**, *231*, 583–599. [[CrossRef](#)]
20. Vijay, K.G.; Venkateswarlu, V.; Nishad, C.S. Wave scattering by inverted trapezoidal porous boxes using dual boundary element method. *Ocean Eng.* **2021**, *219*, 108149. [[CrossRef](#)]
21. Fouladi, M.Q.; Badieli, P.; Vahdani, S. A study on full interaction of water waves with moored rectangular floating breakwater by applying 2DV scaled boundary finite element method. *Ocean Eng.* **2021**, *220*, 108450. [[CrossRef](#)]
22. Peng, W.; Lee, K.-H.; Shin, S.-H.; Mizutani, N. Numerical simulation of interactions between water waves and inclined-moored submerged floating breakwaters. *Coast. Eng.* **2013**, *82*, 76–87. [[CrossRef](#)]
23. Qu, K.; Sun, W.Y.; Kraatz, S.; Deng, B.; Jiang, C.B. Effects of floating breakwater on hydrodynamic load of low-lying bridge deck under impact of cnoidal wave. *Ocean Eng.* **2020**, *203*, 107217. [[CrossRef](#)]
24. Zhan, J.-M.; Chen, X.-B.; Gong, Y.-J.; Hu, W.-Q. Numerical investigation of the interaction between an inverse T-type fixed/floating breakwater and regular/irregular waves. *Ocean Eng.* **2017**, *137*, 110–119. [[CrossRef](#)]
25. Zhang, H.; Zhou, B.; Vogel, C.; Willden, R.; Zang, J.; Zhang, L. Hydrodynamic performance of a floating breakwater as an oscillating-buoy type wave energy converter. *Appl. Energy* **2020**, *257*, 113996. [[CrossRef](#)]
26. Monaghan, J.J. Smoothed particle hydrodynamics. *Annu. Rev. Astron. Astrophys.* **1992**, *30*, 543–574. [[CrossRef](#)]
27. Monaghan, J.J. Smoothed particle hydrodynamics. *Rep. Prog. Phys.* **2005**, *68*, 1703–1759. [[CrossRef](#)]
28. Zhang, A.-M.; Sun, P.-N.; Ming, F.-R.; Colagrossi, A. Smoothed particle hydrodynamics and its applications in fluid-structure interactions. *J. Hydrodyn.* **2017**, *29*, 187–216. [[CrossRef](#)]
29. Gomez-Gesteira, M.; Rogers, B.D.; Dalrymple, R.A.; Crespo, A.J.C. State-of-the-art of classical SPH for free-surface flows. *J. Hydraul. Res.* **2010**, *48*, 6–27. [[CrossRef](#)]
30. Liu, M.B.; Liu, G.R. Smoothed particle hydrodynamics (SPH): An overview and recent developments. *Arch. Comput. Methods Eng.* **2010**, *17*, 25–76. [[CrossRef](#)]
31. Lucy, L.B. A numerical approach to the testing of the fission hypothesis. *Astron. J.* **1977**, *82*, 1013–1024. [[CrossRef](#)]
32. Gingold, R.A.; Monaghan, J.J. Smoothed particle hydrodynamics: Theory and application to non-spherical stars. *Mon. Not. R. Astron. Soc.* **1977**, *181*, 375–389. [[CrossRef](#)]

33. Monaghan, J.J.; Rafiee, A. A simple SPH algorithm for multi-fluid flow with high density ratios. *Int. J. Numer. Methods Fluids* **2013**, *71*, 537–561. [[CrossRef](#)]
34. Monaghan, J.J. Simulating free surface flows with SPH. *J. Comput. Phys.* **1994**, *110*, 399–406. [[CrossRef](#)]
35. Shao, S.; Lo, E.Y.M. Incompressible SPH method for simulating Newtonian and non-Newtonian flows with a free surface. *Adv. Water Resour.* **2003**, *26*, 787–800. [[CrossRef](#)]
36. Gray, J.P.; Monaghan, J.J.; Swift, R.P. SPH elastic dynamics. *Comput. Meth. Appl. Mech. Eng.* **2001**, *190*, 6641–6662. [[CrossRef](#)]
37. Bui, H.H.; Fukagawa, R.; Sako, K.; Ohno, S. Lagrangian meshfree particles method (SPH) for large deformation and failure flows of geomaterial using elastic-plastic soil constitutive model. *Int. J. Numer. Anal. Methods Geomech.* **2008**, *32*, 1537–1570. [[CrossRef](#)]
38. Liu, M.B.; Liu, G.R.; Lam, K.Y.; Zong, Z. Smoothed particle hydrodynamics for numerical simulation of underwater explosion. *Comput. Mech.* **2003**, *30*, 106–118. [[CrossRef](#)]
39. Alaa, G.; Francomanob, E.; Tortoricib, A.; Toscanob, E.; Viola, F. Smoothed Particle ElectroMagnetics: A mesh-free solver for transients. *J. Comput. Appl. Math.* **2006**, *191*, 194–205. [[CrossRef](#)]
40. Ming, F.R.; Zhang, A.M.; Cheng, H.; Sun, P.N. Numerical simulation of a damaged ship cabin flooding in transversal waves with Smoothed Particle Hydrodynamics method. *Ocean Eng.* **2018**, *165*, 336–352. [[CrossRef](#)]
41. Shi, Y.; Li, S.; Chen, H.; He, M.; Shao, S. Improved SPH simulation of spilled oil contained by flexible floating boom under wave-current coupling condition. *J. Fluids Struct.* **2018**, *76*, 272–300. [[CrossRef](#)]
42. Bouscasse, B.; Colagrossi, A.; Marrone, S.; Souto-Iglesias, A. SPH modelling of viscous flow past a circular cylinder interacting with a free surface. *Comput. Fluids* **2017**, *146*, 190–212. [[CrossRef](#)]
43. Luo, M.; Reeve, D.E.; Shao, S.; Karunarathna, H.; Lin, P.; Cai, H. Consistent Particle Method simulation of solitary wave impinging on and overtopping a seawall. *Eng. Anal. Bound. Elem.* **2019**, *103*, 160–171. [[CrossRef](#)]
44. Ren, Y.; Luo, M.; Lin, P. Consistent Particle Method simulation of solitary wave interaction with a submerged breakwater. *Water* **2019**, *11*, 261. [[CrossRef](#)]
45. Wang, D.; Liu, P.L.-F. An ISPH with  $k-\epsilon$  closure for simulating turbulence under solitary waves. *Coast. Eng.* **2020**, *157*, 103657. [[CrossRef](#)]
46. Zheng, X.; You, Y.; Ma, Q.; Khayyer, A.; Shao, S. A comparative study on violent sloshing with complex baffles using the ISPH method. *Appl. Sci.* **2018**, *8*, 904. [[CrossRef](#)]
47. Delorme, L.; Colagrossi, A.; Souto-Iglesias, A.; Zamora-Rodríguez, R.; Botía-Vera, E. A set of canonical problems in sloshing, Part I: Pressure field in forced roll—comparison between experimental results and SPH. *Ocean Eng.* **2009**, *36*, 168–178. [[CrossRef](#)]
48. Chen, Z.; Zong, Z.; Li, H.T.; Li, J. An investigation into the pressure on solid walls in 2D sloshing using SPH method. *Ocean Eng.* **2013**, *59*, 129–141. [[CrossRef](#)]
49. Gómez-Gesteira, M.; Cerqueiro, D.; Crespo, C.; Dalrymple, R. Green water overtopping analyzed with a SPH model. *Ocean Eng.* **2005**, *32*, 223–238. [[CrossRef](#)]
50. He, M.; Gao, X.; Xu, W.; Ren, B.; Wang, H. Potential application of submerged horizontal plate as a wave energy breakwater: A 2D study using the WCSPH method. *Ocean Eng.* **2019**, *185*, 27–46. [[CrossRef](#)]
51. Wen, H.; Ren, B.; Yu, X. An improved SPH model for turbulent hydrodynamics of a 2D oscillating water chamber. *Ocean Eng.* **2018**, *150*, 152–166. [[CrossRef](#)]
52. Manenti, S.; Sibilla, S.; Gallati, M.; Agate, G.; Guandalini, R. SPH simulation of sediment flushing induced by a rapid water flow. *J. Hydraul. Eng.* **2012**, *138*, 272–284. [[CrossRef](#)]
53. Shi, H.; Yu, X.; Dalrymple, R.A. Development of a two-phase SPH model for sediment laden flows. *Comput. Phys. Commun.* **2017**, *221*, 259–272. [[CrossRef](#)]
54. Wang, D.; Li, S.; Arikawa, T.; Gen, H. ISPH simulation of scour behind seawall due to continuous tsunami overflow. *Coast. Eng. J.* **2016**, *58*, 1650014. [[CrossRef](#)]
55. Gotoh, H.; Khayyer, A. Current achievements and future perspectives for projection-based particle methods with applications in ocean engineering. *J. Ocean Eng. Mar. Energy* **2016**, *2*, 251–278. [[CrossRef](#)]
56. Gotoh, H.; Khayyer, A. On the state-of-the-art of particle methods for coastal and ocean engineering. *Coast. Eng. J.* **2018**, *60*, 79–103. [[CrossRef](#)]
57. Luo, M.; Khayyer, A.; Lin, P. Particle methods in ocean and coastal engineering. *Appl. Ocean Res.* **2021**, *114*, 102734. [[CrossRef](#)]
58. Domínguez, J.M.; Fourtakas, G.; Altomare, C.; Canelas, R.B.; Tafuni, A.; García-Feal, O.; Martínez-Estévez, I.; Mokos, A.; Vacondio, R.; Crespo, A.J.C.; et al. DualSPHysics: From fluid dynamics to multiphysics problems. *Comput. Part. Mech.* **2021**, 1–29. [[CrossRef](#)]
59. SPlisHSPlasH Library. Available online: <https://github.com/InteractiveComputerGraphics/SPlisHSPlasH> (accessed on 6 September 2021).
60. Zhang, C.; Rezavand, M.; Zhu, Y.; Yu, Y.; Wu, D.; Zhang, W.; Wang, J.; Hu, X. SPHinXsys: An open-source multi-physics and multi-resolution library based on smoothed particle hydrodynamics. *Comput. Phys. Commun.* **2021**, *267*, 108066. [[CrossRef](#)]
61. Gomez-Gesteira, M.; Rogers, B.D.; Crespo, A.J.C.; Dalrymple, R.A.; Narayanaswamy, M.; Dominguez, J.M. SPHysics—Development of a free-surface fluid solver—Part 1: Theory and formulations. *Comput. Geosci.* **2012**, *48*, 289–299. [[CrossRef](#)]
62. Rogers, B.D.; Dalrymple, R.A.; Stansby, P.K. Simulation of caisson breakwater movement using 2-D SPH. *J. Hydraul. Res.* **2010**, *48*, 135–141. [[CrossRef](#)]

63. Wang, Y.-Z.; Chen, N.-N.; Chi, L.-H. Numerical simulation on joint motion process of various modes of caisson breakwater under wave excitation. *Commun. Numer. Methods Eng.* **2006**, *22*, 535–545.
64. Akbari, H.; Taherkhani, A. Numerical study of wave interaction with a composite breakwater located on permeable bed. *Coast. Eng.* **2019**, *146*, 1–13. [[CrossRef](#)]
65. Altomare, C.; Crespo, A.J.C.; Rogers, B.D.; Dominguez, J.M.; Gironella, X.; Gómez-Gesteira, M. Numerical modelling of armour block sea breakwater with smoothed particle hydrodynamics. *Comput. Struct.* **2014**, *130*, 34–45. [[CrossRef](#)]
66. Zhang, F.; Crespo, A.; Altomare, C.; Dominguez, J.; Marzeddu, A.; Shang, S.-P.; Gómez-Gesteira, M. DualSPHysics: A numerical tool to simulate real breakwaters. *J. Hydrodyn.* **2018**, *30*, 95–105. [[CrossRef](#)]
67. Ren, B.; Jin, Z.; Gao, R.; Wang, Y.-X.; Xu, Z.-L. SPH-DEM modeling of the hydraulic stability of 2D blocks on a slope. *J. Waterw. Port Coast. Ocean Eng.* **2014**, *140*, 04014022. [[CrossRef](#)]
68. Sarfaraz, M.; Pak, A. Numerical investigation of the stability of armour units in low-crested breakwaters using combined SPH–Polyhedral DEM method. *J. Fluids Struct.* **2018**, *81*, 14–35. [[CrossRef](#)]
69. Shao, S.; Gotoh, H. Simulating coupled motion of progressive wave and floating curtain wall by SPH-LES model. *Coast. Eng. J.* **2004**, *46*, 171–202. [[CrossRef](#)]
70. Ren, B.; He, M.; Li, Y.; Dong, P. Application of smoothed particle hydrodynamics for modeling the wave-moored floating breakwater interaction. *Appl. Ocean Res.* **2017**, *67*, 277–290. [[CrossRef](#)]
71. Domínguez, J.M.; Crespo, A.J.C.; Hall, M.; Altomare, C.; Wu, M.; Stratigaki, V.; Troch, P.; Cappiotti, L.; Gómez-Gesteira, M. SPH simulation of floating structures with moorings. *Coast. Eng.* **2019**, *153*, 103560. [[CrossRef](#)]
72. Hall, M.; Goupee, A. Validation of a lumped-mass mooring line model with DeepCwind semisubmersible model test data. *Ocean Eng.* **2015**, *104*, 590–603. [[CrossRef](#)]
73. Liu, Z.; Wang, Y. Numerical studies of submerged moored box-type floating breakwaters with different shapes of cross-sections using SPH. *Coast. Eng.* **2020**, *158*, 103687. [[CrossRef](#)]
74. Cui, J.; Chen, X.; Sun, P. Numerical investigation on the hydrodynamic performance of a new designed breakwater using smoothed particle hydrodynamic method. *Eng. Anal. Bound. Elem.* **2021**, *130*, 379–403. [[CrossRef](#)]
75. Masciola, M.; Jonkman, J.; Robertson, A. Implementation of a multisegmented, quasi-static cable model. In Proceedings of the 23rd International Offshore and Polar Engineering Conference, Anchorage, AK, USA, 30 June–5 July 2013; International Society of Offshore and Polar Engineers: Cupertino, CA, USA, 2013; pp. 315–322.
76. Gunn, D.F.; Rudman, M.; Cohen, R.C.Z. Wave interaction with a tethered buoy: SPH simulation and experimental validation. *Ocean Eng.* **2018**, *156*, 306–317. [[CrossRef](#)]
77. Pan, K.; Ijzermans, R.H.A.; Jones, B.D.; Thyagarajan, A.; Van Beest, B.W.H.; Williams, J.R. Application of the SPH method to solitary wave impact on an offshore platform. *Comput. Part. Mech.* **2016**, *3*, 155–166. [[CrossRef](#)]
78. Rudman, M.; Cleary, P.W. The influence of mooring system in rogue wave impact on an offshore platform. *Ocean Eng.* **2016**, *115*, 168–181. [[CrossRef](#)]
79. Barreiro, A.; Crespo, A.J.C.; Dominguez, J.M.; Garcia-Feal, O.; Zabala, I.; Gomez-Gesteira, M. Quasi-static mooring solver implemented in SPH. *J. Ocean Eng. Mar. Energy* **2016**, *2*, 381–396. [[CrossRef](#)]
80. Crespo, A.J.C.; Altomare, C.; Domínguez, J.M.; González-Cao, J.; Gómez-Gesteira, M. Towards simulating floating offshore oscillating water column converters with Smoothed Particle Hydrodynamics. *Coast. Eng.* **2017**, *126*, 11–26. [[CrossRef](#)]
81. Ardianti, A.; Mutsuda, H.; Kawawaki, K.; Doi, Y.; Fukuhara, T. Characteristic of tsunami force acting on shelter with mooring. *Appl. Ocean Res.* **2017**, *64*, 70–85. [[CrossRef](#)]
82. Antuono, M.; Colagrossi, A.; Marrone, S.; Molteni, D. Free-surface flows solved by means of SPH schemes with numerical diffusive terms. *Comput. Phys. Commun.* **2010**, *181*, 532–549. [[CrossRef](#)]
83. Antuono, M.; Colagrossi, A.; Marrone, S. Numerical diffusive terms in weakly-compressible SPH schemes. *Comput. Phys. Commun.* **2012**, *183*, 2570–2580. [[CrossRef](#)]
84. Wendland, H. Piecewise polynomial, positive definite and compactly supported radial functions of minimal degree. *Adv. Comput. Math.* **1995**, *4*, 389–396. [[CrossRef](#)]
85. He, M.; Khayyer, A.; Gao, X.; Xu, W.; Liu, B. Theoretical method for generating solitary waves using plunger-type wavemakers and its Smoothed Particle Hydrodynamics validation. *Appl. Ocean Res.* **2021**, *106*, 102414. [[CrossRef](#)]
86. Ren, B.; He, M.; Dong, P.; Wen, H. Nonlinear simulations of wave-induced motions of a freely floating body using WCSPH method. *Appl. Ocean Res.* **2015**, *50*, 1–12. [[CrossRef](#)]
87. He, M.; Xu, W.; Gao, X.; Ren, B. SPH simulation of wave scattering by a heaving submerged horizontal plate. *Int. J. Ocean Coast. Eng.* **2018**, *1*, 1840004. [[CrossRef](#)]
88. Shi, Y.; Li, S.; Peng, S.; Chen, H.; He, M. Numerical modeling of flexible floating boom using a coupled SPH–FEM model. *Coast. Eng. J.* **2018**, *60*, 140–158. [[CrossRef](#)]
89. Yang, C.; Weller, S.D.; Wang, Y.-X.; Ning, D.-Z.; Johanning, L. Experimental and numerical investigation on coupled motion characteristics of a tunnel element suspended from a twin-barge. *Ocean Eng.* **2018**, *153*, 201–214. [[CrossRef](#)]
90. Hirakuchi, H.; Kajima, R.; Kawaguchi, T. Application of a piston-type absorbing wavemaker to irregular wave experiments. *Coast. Eng. Jpn.* **1990**, *33*, 11–24. [[CrossRef](#)]
91. Carmigniani, R.A.; Violeau, D. Optimal sponge layer for water waves numerical models. *Ocean Eng.* **2018**, *163*, 169–182. [[CrossRef](#)]

92. Goda, Y.; Suzuki, Y. Estimation of incident and reflected waves in random wave experiments. In Proceedings of the 15th Conference on Coastal Engineering, Honolulu, HI, USA, 11–17 July 1976; American Society of Civil Engineers: New York, NY, USA, 1977; pp. 828–845.
93. Ji, C.; Cheng, Y.; Cui, J.; Yuan, Z.; Gaidai, O. Hydrodynamic performance of floating breakwaters in long wave regime: An experimental study. *Ocean Eng.* **2018**, *152*, 154–166. [[CrossRef](#)]
94. Antuono, M.; Colagrossi, A.; Marrone, S.; Lugni, C. Propagation of gravity waves through an SPH scheme with numerical diffusive terms. *Comput. Phys. Commun.* **2011**, *182*, 866–877. [[CrossRef](#)]
95. Altomare, C.; Domínguez, J.M.; Crespo, A.J.C.; González-Cao, J.; Suzuki, T.; Gómez-Gesteira, M.; Troch, P. Long-crested wave generation and absorption for SPH-based DualSPHysics model. *Coast. Eng.* **2017**, *127*, 37–54. [[CrossRef](#)]
96. Hall, M.; Buckham, B.; Crawford, C. Evaluating the importance of mooring line model fidelity in floating offshore wind turbine simulations. *Wind Energy* **2014**, *17*, 1835–1853. [[CrossRef](#)]
97. Davidson, J.; Ringwood, J.V. Mathematical modelling of mooring systems for wave energy converters—A Review. *Energies* **2017**, *10*, 666. [[CrossRef](#)]